

This article appeared in a journal published by Elsevier. The attached copy is furnished to the author for internal non-commercial research and education use, including for instruction at the authors institution and sharing with colleagues.

Other uses, including reproduction and distribution, or selling or licensing copies, or posting to personal, institutional or third party websites are prohibited.

In most cases authors are permitted to post their version of the article (e.g. in Word or Tex form) to their personal website or institutional repository. Authors requiring further information regarding Elsevier's archiving and manuscript policies are encouraged to visit:

<http://www.elsevier.com/copyright>



Contents lists available at ScienceDirect

Combustion and Flame

journal homepage: www.elsevier.com/locate/combustflame

Numerical simulation and experiments of burning douglas fir trees

William Mell *, Alexander Maranghides, Randall McDermott, Samuel L. Manzello

Building and Fire Research Laboratory, National Institute of Standards and Technology, Gaithersburg, MD, USA

ARTICLE INFO

Article history:

Received 31 January 2009

Received in revised form 12 March 2009

Accepted 13 June 2009

Available online 25 July 2009

Keywords:

CFD

Fire spread

Wildland fire

Numerical simulation

Large-eddy simulation

ABSTRACT

Fires spreading in elevated vegetation, such as chaparral or pine forest canopies, are often more intense than fires spreading through surface vegetation such as grasslands. As a result, they are more difficult to suppress, produce higher heat fluxes, more firebrands and smoke, and can interact with, or create, local weather conditions that lead to dangerous fire behavior. Such wildland fires can pose a serious threat to wildland–urban interface communities. A basic building block of such fires is a single tree. In the work presented here, a number of individual trees, of various characteristics, were burned without an imposed wind in the Large Fire Laboratory of the National Institute of Standards and Technology. A numerical model capable of representing the spatial distribution of vegetation in a tree crown is presented and evaluated against tree burning experiments. For simplicity, the vegetation was assumed to be uniformly distributed in a tree crown represented by a well defined geometric shape (cone or cylinder). Predictions of the time histories of the radiant heat flux and mass loss rates for different fuel moisture contents and tree heights compared favorably to measured values and trends. This work is a first step toward the development and application of a physics-based computer model to spatially complex, elevated, vegetation present in forest stands and in the wildland–urban interface.

Published by Elsevier Inc. on behalf of The Combustion Institute.

1. Introduction and background

Vegetative fuels and fires in a wildland setting can be categorized into ground, surface, or crown types (e.g., Chap. 4 in [1]). From a modeling point of view, a distinguishing feature of fires is the flame height above the vegetative fuel bed. In fires with flame heights that are significantly larger than the height of the fuel bed most flaming combustion will take place above the fuel bed. This can occur, for example, in many high intensity grass fires. In such scenarios, there is justification for using separate computational grids for the fire plume (coarser grid) and the vegetation (finer grid). This is especially useful for simulations over large domains (hundreds of meters on a side) since computational costs can be reduced. Such an approach was implemented recently and applied to Australian grassland fuels [2].

In scenarios where the fire plume height is of the same scale as, or smaller than, the fuel bed height, or spatial inhomogeneities in the fuel bed are significant compared to the depth of the fire (i.e., the extent of the fire parallel to the direction of firespread), another approach is required in order to more fully capture the interaction between the fire and the vegetative fuels. Such scenarios can include fire spread through complex arrangements of surface, mid-

storey, and crown fuels each with varied fuel loading. A specific example is the initial stage of vertical flame spread for fires that ignite near the base of the vegetation column and spread upward. Another example is changes in the horizontal distribution of fuels (clumping or spottiness) since the fire can “drop down” from raised fuels, spread along surface fuels, and then spread upward again into the raised fuels. These fuel scenarios, while realistic and relevant, are outside the realm of application of one-dimensional fire spread models such as that developed by Rothermel [3] which is used in BEHAVE [4] and FARSITE [5].

Variations in fuel loading is an important consideration in devising and assessing fuel treatments, determining the fire intensity of a prescribed fire, understanding the processes involved in transition from surface to crown fires, and assessing fire risk in the wildland–urban interface (WUI). Fuels in the WUI are inherently inhomogeneous in type and spatial distribution, with a mixture of structural fuels and indigenous, as well as ornamental, vegetation. The National Institute of Standards and Technology (NIST) is currently seeking to develop a better understanding of fire behavior in the WUI. This project includes laboratory experiments, field measurements (post WUI fire analysis; heat, wind, and temperature during prescribed fires), fire behavior modeling, and economic modeling all focused on the WUI problem. A number of fire behavior modeling approaches are being pursued. The numerical model developed and tested here is weighted toward a more complete inclusion of the physical processes, as opposed to a more semi-empirical approach (e.g., see [6]). The present work is a first

* Corresponding author.

E-mail addresses: ruddy@nist.gov (W. Mell), alex@nist.gov (A. Maranghides), randall.mcdermott@nist.gov (R. McDermott), samuel.manzello@nist.gov (S.L. Manzello).

Nomenclature

Variable	Description, Units		
A	frontal area of fuel element, m^2	Δh_c	mass-based heat of combustion, kJ kg^{-1}
C_D	drag coefficient	Δh_{pyr}	heat of pyrolysis, kJ kg^{-1}
$C_{\text{EDC}} = 0.1$	Eddy Dissipation Concept (EDC) model constant	Δh_{vap}	heat of vaporization, kJ kg^{-1}
c_p	specific heat at constant pressure, $\text{kJ kg}^{-1} \text{K}^{-1}$	Δm	mass loss, kg
D	mass diffusivity, $\text{m}^2 \text{s}^{-1}$	$\Delta x, \Delta y, \Delta z$	grid spacing, m
f_D'''	drag force per unit volume, $\text{kg m}^{-2} \text{s}^{-2}$	$\delta(\mathbf{x})$	Dirac delta function, m^{-3}
$G(\mathbf{r}; \Delta)$	filter kernel of characteristic width Δ , m^{-3}	κ	radiative absorption coefficient
$h = \sum_i Y_i h_i$	mixture enthalpy, kJ kg^{-1}	μ	dynamic viscosity of the gaseous mixture, $\text{kg m}^{-1} \text{s}^{-1}$
h_i	specific enthalpy of species i , kJ kg^{-1}	ν_i	stoichiometric coefficient of species i
\mathbf{I}	identity matrix	ρ	mass density, kg m^{-3}
$I(\mathbf{x}, \hat{\mathbf{s}})$	radiation intensity, $\text{W MHz m}^{-2} \text{sr}^{-1}$	σ_e	surface-to-volume ratio for fuel elements of type e , m^{-1}
$I_b(\mathbf{x}, \hat{\mathbf{s}})$	blackbody radiation intensity, $\text{W MHz m}^{-2} \text{sr}^{-1}$	$\sigma_B = 5.67 \times 10^{-11}$	Stefan–Boltzmann constant, $\text{kW m}^{-2} \text{K}^{-4}$
\mathbf{J}	diffusive mass flux, $\text{kg m}^{-2} \text{s}$	τ	stress tensor, Pa
k	thermal conductivity, $\text{W m}^{-1} \text{K}^{-1}$	χ_{char}	fraction of virgin solid fuel converted to char
m	mass, kg	χ_r	fraction of local chemical heat release radiated to surroundings
\dot{m}_i'''	chemical mass consumption of gas species i , $\text{kg m}^{-3} \text{s}^{-1}$	χ_s	fraction of consumed fuel mass converted to soot
\dot{m}_b'''	mass production due to thermal degradation of vegetation, $\text{kg m}^{-3} \text{s}^{-1}$		
M	fuel moisture content of vegetation		
N	number of fuel elements		
W_i	molecular weight of gas species i , kg kmol^{-1}		
$W = (\sum_i Y_i / W_i)^{-1}$	average molecular weight of gas mixture, kg kmol^{-1}		
$\hat{\mathbf{n}}$	unit normal vector		
\dot{Q}_c'''	heat release rate per unit volume due to chemical reactions, kW m^{-3}		
p	hydrodynamic pressure, Pa		
p_0	thermodynamic pressure, Pa		
\dot{q}_{net}'''	conductive plus radiative heat source, kW m^{-3}		
\mathbf{q}	heat flux vector, kW m^{-2}		
$\hat{\mathbf{s}}$	unit vector in direction of radiation intensity		
Re	Reynolds number		
r	radius or stoichiometric ratio or m		
T	temperature, $^\circ\text{C}$		
\mathbf{u}	velocity vector, m s^{-1}		
U	integrated radiation intensity, W m^{-2}		
V	volume, m^3		
\mathbf{x}	position vector, m		
$Y_i = \rho_i / \rho$	mass fraction of species i		
S	surface area, m^2		
$\beta = \rho_{\text{bv}} / \rho_e$	packing ratio		
ΔH_c	molar heat of combustion, kJ kmol^{-1}		

Subscripts

a	ambient
b	bulk vegetative fuel quantity or blackbody
c	convective, combustion, chemical
D	drag
e	fuel element type
i	gaseous species
k	fuel element index
r	radiative
v	virgin dry vegetation
F	fuel species
t	turbulent

Superscripts

d	deviatoric part
sgs	subgrid scale

Special operators

$\bar{\phi}(\mathbf{x}, t) \equiv \int G(\mathbf{x} - \mathbf{x}') \phi(\mathbf{x}', t) d\mathbf{x}'$	conventional implicit spatial filter
$\tilde{\phi}(\mathbf{x}, t) \equiv \overline{\rho(\mathbf{x}, t) \phi(\mathbf{x}, t)} / \overline{\rho(\mathbf{x}, t)}$	implicit Favre-filter
$\langle \phi(\mathbf{x}, t) \rangle_{V_b} \equiv \frac{1}{V_b} \int_{x-\Delta x/2}^{x+\Delta x/2} \int_{y-\Delta y/2}^{y+\Delta y/2} \int_{z-\Delta z/2}^{z+\Delta z/2} \phi(\mathbf{x}', t) d\mathbf{x}' d\mathbf{y}' d\mathbf{z}'$	explicit anisotropic box filter
$\tilde{D}\phi/\tilde{D}t \equiv \partial\phi/\partial t + \tilde{\mathbf{u}} \cdot \nabla\phi$	Favre-filtered material derivative

step in the development of a validated physics-based numerical model for simulating fire spread through trees (crown fuel type).

The model presented here numerically solves the governing equations for fluid flow, combustion, heat transfer, and thermal degradation of the vegetative fuel. This results in a three-dimensional, time-dependent, prediction of fire behavior. Measurements from experiments of burning Douglas firs are used to validate the numerical predictions. The targeted application area is the simulation of fire behavior through the wildland–urban interface. The end goal is to develop a range of computationally efficient tools to help land managers and others assess wildland fire risk to communities and homes. A suitably validated physics-based approach has the potential to account for realistic variations in the environmental conditions relevant to WUI fire behavior. At present, rule-based checklists or limited empirical studies are used to reduce or assess the risk of structures to WUI fires (specific examples may be found in standards and codes [7,8] or an overview in Mell et al. [9]).

The next section provides an overview of the model (a short derivation of the model equations is given in Appendix A). Next,

the Douglas fir burn experiments conducted at NIST are described and results are presented. This is followed by model predictions of experimental tree burns and their comparison to experimental findings. The paper ends with a summary and conclusions regarding the performance of the model and future work.

2. Overview of the numerical model

The numerical approach, called WFDS for WUI Fire Dynamics Simulator, is an extension of the capabilities of the FDS5 (Fire Dynamics Simulator version 5.2) to outdoor fire spread and smoke transport problems that include vegetative and structural fuels and complex terrain. FDS is a fire behavior model developed by NIST in cooperation with VTT Technical Research Center of Finland, industry, and academics. To date, the focus of FDS has been to simulate stationary outdoor fires (e.g., pool fires and tank farm fires) and structural fires. The methods of computational fluid dynamics (CFD) are used to solve the three-dimensional (or two-dimensional) time-dependent equations governing fluid motion, com-

bustion, and heat transfer. Throughout the course of the development of FDS, experiments conducted in NIST's Large Fire Laboratory and elsewhere have been used to evaluate and further refine the modeling approach (see McGrattan et al. [10] for information on FDS validation studies; and McDermott et al. [11] for verification studies). An FDS technical manual [12] and user guide [13] are also available.

The numerical model is based on the large-eddy simulation (LES) approach and provides a time-dependent, coarse-grained numerical solution to the governing transport equations for mass, momentum, and energy. The effect of thermal expansion due to chemical reaction and heat and mass transfer enters the computation through an elliptic constraint, derived using the energy equation, on the velocity field. The local mean temperature is then obtained via the ideal gas equation of state. Dissipation of kinetic energy is achieved through a simple closure for the turbulent stress: the constant coefficient Smagorinsky model. The turbulent transport of heat and mass is accounted for by use of constant turbulent Prandtl and Schmidt numbers, respectively. The subgrid heterogeneity of species concentrations and temperature is treated in conjunction with the reaction, heat transfer, and radiation intensity models. Where these effects are important they are included using empirical correlations.

The advective form of the continuity equation is solved together with the Stokes form of the momentum equations on a structured Cartesian staggered grid. The spatial discretizations are second-order accurate for uniform grids. Species mass equations are advanced using a modified version of MacCormack's predictor-corrector scheme and the momentum equations are advanced using a two-stage projection scheme based on the explicit modified Euler method. Combustion heat release rate is modeled based on the Eddy Dissipation Concept (EDC) model of Magnussen [14].

The solid phase model is similar to models used by previous researchers. In particular, Albini [15,16] presented similar model equations for two-dimensional heat transfer in a medium containing vegetation and air under an assumed heat flux due to an idealize fire shape. Albini's approach provided a fire spread rate but did not model the pyrolysis or char oxidation of the solid fuel. More recently, similar models for the heat transfer within the vegetative fuel bed have been incorporated in CFD models, which include (to differing levels of approximations) thermal degradation (pyrolysis and char oxidation) and gas-phase combustion, to obtain a more complete approach to predicting the transient behavior of the fire and its buoyant plume (for example [17,18,2]). A review of these methods is given in Mell et al. [2].

A tree crown is assumed to be composed of fixed, thermally thin, optically black, fuel elements. More than one type of thermally thin element (e.g., foliage and thermally thin roundwood) can be represented. Note that an emissivity of 0.9 is characteristic of wildland vegetation [19] so the assumption that a fuel element is a perfect absorber is reasonable. The thermally thin assumption is commonly used in fire spread models involving fine wildland fuels (grass and foliage of shrubs and trees) [3]. Experiments have been conducted [20,21] and are ongoing to measure the fire brand generation properties of Douglas fir and their transport properties in controlled wind environments. Vegetation that is thermally thin is sufficiently small in size (e.g., branches <6 mm in diameter) that it is not resolved on the computational grids used here (\varnothing (10) cm). In the approach used here the thermal, radiative, and drag processes are determined from the bulk vegetative properties (e.g., bulk density). This is similar to other modeling approaches [17,22–24].

Although the tree crown can be built cell by cell on the computational grid, for simplicity it is approximated as a simple geometric shape (cone or cylinder) with a uniform distribution of bulk fuel. For consistency this requires farm grown experimental trees

that were more uniform in their spatial distribution of foliage, and other thermally thin fuels, than usually occurs in a natural forest setting. The use of trees with a relatively uniform spatial distribution of crown bulk density, on the scale of \varnothing (10) cm, greatly simplifies the validation of WFDS and experimental procedures. The influence of non-uniform spatial distribution of crown fuel on fire behavior will be considered at a later date. An example of approximating a tree crown as either a cone or a cylinder is shown Fig. 1a. The outlines of both a conical and cylindrical volume overlaid on a photograph of one of the 5 m tall experimental trees. A white square, labeled “ \approx grid cell”, represents a 10 cm WFDS grid cell, which is characteristic of the grid cells used in the simulations. The approximation of uniformly distributing the unresolved vegetative mass, foliage and roundwood, within a grid cell is shown in Fig. 1b.

Both convective and radiative heat transfer between the gas phase and the vegetation is accounted for, as is the drag of the vegetation on the airflow. In general, as the temperature of a vegetative fuel increases, first moisture is removed, followed by pyrolysis (the generation of fuel vapors), and then char oxidation (also known as smoldering combustion). In the modeling approach used here, the temperature equation for the fuel bed is solved assuming a two stage endothermic decomposition process of water evaporation followed by solid fuel pyrolysis.

Char oxidation requires sufficiently high solid temperatures and gas-phase oxygen concentrations. From observations of the laboratory tree burns, mass consumption and heat release due to char oxidation is not relevant until after the peak mass loss rate. For example, Fig. 2b is a snapshot of an experiment at the point of maximum mass loss rate. The entire crown appears to be engulfed by flaming combustion (i.e., it appears that combustion is occurring throughout the crown). Fig. 2d is a WFDS prediction of the oxygen mass fraction in a slice plane passing through the center of the simulated tree crown. The WFDS cone-shaped approximation to the tree crown can be seen. This figure shows that there is insufficient oxygen to support flaming combustion or char oxidation within simulated tree crown. Instead, the crown is surrounded by a band of flaming combustion. Thus, any significant char oxidation modeled in WFDS would not take place until the flaming combustion subsided, exposing the solid fuel to oxygen. Char oxidation (glowing combustion) can clearly be seen in the experiments after flaming combustion subsides in Fig. 2c. Since the current focus of WFDS model development is the prediction of flame spread through vegetation, char oxidation is not modeled here.

3. Tree burn experiments

The tree burning experiments reported here were conducted in NIST's Large Fire Laboratory (LFL). Douglas fir was selected as the tree species for these experiments because it was readily available in local tree farms and is abundant in the western United States of America where WUI fires are most prevalent [25,26]. A schematic showing the different measures used to describe a tree is shown in Fig. 3. Trees of two different heights were burned: approximately 2 m and 5 m. The trees were selected from a local nursery, cut (no roots were present), and delivered to NIST. The trees were mounted on custom stands and allowed to dry. During the experiments, no wind was imposed on the trees. Samples were selected from random locations in the tree crown for determining moisture content. The moisture content of the tree was measured using a Computrac XL1000 moisture meter.¹ A calibration of the moisture

¹ Any mention of commercial products is for information only; it does not imply recommendation or endorsement by NIST, nor does it imply that the products identified are necessarily the best available for the purpose.

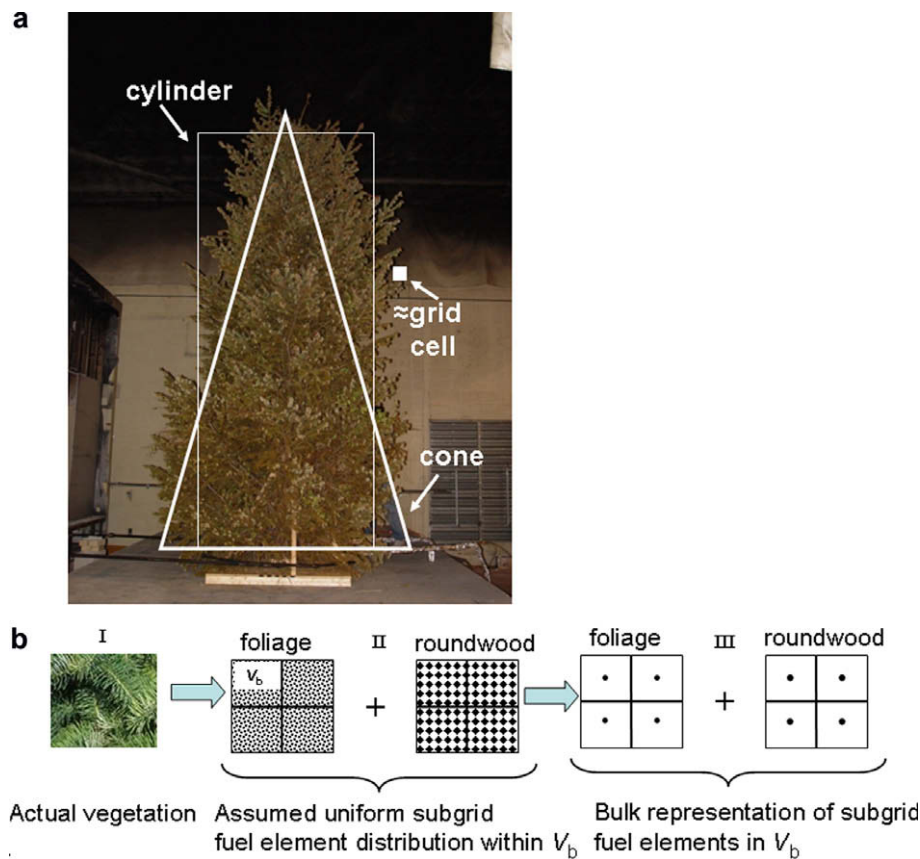


Fig. 1. (a) Photograph of 5 m tall Douglas fir with the outlines of the cross sections of both a conical and a cylindrical volume approximation to the tree crown. For simplicity the WFDS model approximates the tree as a cone or a cylinder. The approximate size of a WFDS grid cell ($\delta x = 10$ cm) is also shown. (b) Illustration of the approach used in WFDS to model the subgrid vegetative mass. (b.I) A photo of the actual vegetation. (b.II) The vegetation is binned into different types according to size, each of which is assumed to be uniformly distributed through the volume V_b with a bulk density based on measurements. In figure b.II and b.III there are two sizes: foliage and roundwood. The implementation of the model on a computational grid requires an averaging or LES approach shown schematically in b.III. Both II and III show four grid cells, each with volume V_b .

meter was performed, based on oven drying the samples, determining the moisture content, and comparing it to the Computrac moisture measurement. The moisture content obtained from the Computrac meter was within 2% of the oven dried value. The overall uncertainty in the measurements estimated to be $\pm 10\%$. This uncertainty was dependent on the spatial variability within the tree as well as the uncertainty in the analyzer measurement.

Needle samples, as well as small branch samples (three heights, four radial locations at each height), were collected for the moisture measurements. The measurements were taken on a bi-weekly basis. The moisture content, M , determined on a dry basis, is given as a percentage:

$$M = \frac{m_{e,wet} - m_{e,v}}{m_{e,v}} \times 100\%, \quad (1)$$

where $m_{e,wet}$ is the measured mass of the virgin vegetation and $m_{e,v}$ is the mass of the dried virgin vegetation; the subscript e denotes a vegetative fuel element of a given type.

Experimental measurements from nine 2 m tall Douglas fir and three 5 m tall Douglas fir were collected. By design the average moisture levels for the 2 m trees fell into three ranges: $M < 30\%$, $30\% < M < 70\%$, and $70\% < M$. Babrauskas reported that burning characteristics of Douglas fir differed according to these three levels of moisture content [27]. For $M < 30\%$ a tree ignites easily and the fire spreads relatively quickly through the crown, which is often fully consumed. Trees with $30\% < M < 70\%$ are in a transition region, successful ignition results in only partial consumption of the crown. In trees with

$70\% < M$ little burning occurs beyond what is supported by the ignitor used in the experiments. The observed fire behavior in the current experiments is consistent with Babrauskas's observations. At least three replicate burns were conducted for each tree height and moisture content regime.

In general, the moisture-based breakpoints in burning behavior described in the preceding paragraph will depend on the ignition source. Babrauskas, whose focus was on the fire safety issues related to Christmas tree fires in homes, ignited $M < 50\%$ trees with a small single flame and $M > 50\%$ trees with an area fire beneath the crown. Thus, while the moisture dependent burning regimes provide a reasonable data set for model validation, they should be viewed as appropriate to laboratory studies and only cautiously applied to field conditions. Some live fuels, with high moisture contents, can burn due to the presence of high energy volatiles such as terpenes, fats, oils, and waxes. Rothermel has found this to be the case for live chaparral with $M > 100\%$ [28]. Also, in the International Crown Fire Modeling Experiments all foliage and roundwood < 10 mm in diameter was consumed in live crowns with $M > 70\%$ [29]. These tree crowns were subjected to significantly higher heat flux levels, compared to our laboratory trees, from fires spreading through the underlying surface and understory fuels and in nearby tree crowns in the up-spread direction. This intense thermal environment cannot be easily created in a laboratory setting. However, the experiments conducted here do have a controlled, repeatable, procedure for producing well characterized data that can be used to validate a fire spread model at the laboratory scale. The igni-

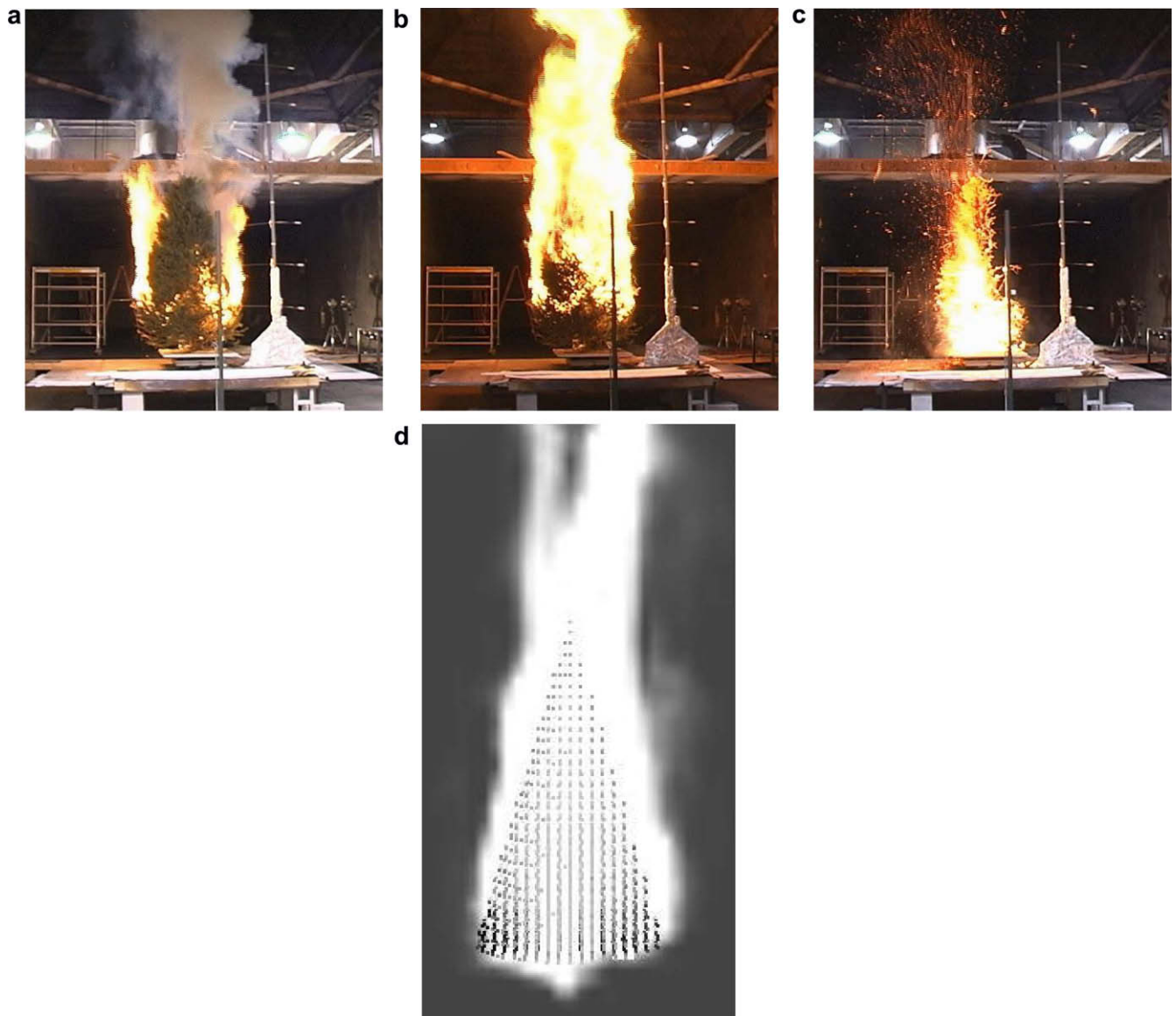


Fig. 2. Photos (a)–(c) show the characteristic evolution of a tree burn experiment for a tree with low moisture content ($M = 26\%$): (a) The fire is established and is spreading up sides of crown. (b) The tree crown is surrounded by flaming combustion. The peak mass loss rate occurs at this point. (c) Flaming has largely subsided except in the lower half of the tree and the burning of downed branches at the base of the tree. Foliage has been completely consumed and the remaining crown is actively smoldering. Note the smoldering firebrands in the air above the crown. (d) A slice plane showing the oxygen mass fraction from the WFDS calculation when the crown is fully surrounded by flaming combustion (i.e., corresponds to burning stage shown in experimental photo (b)). White corresponds to no oxygen and black to an ambient value. The cone shaped approximation to the tree crown can be seen and is completely engulfed in an oxygen free zone.

tion procedure is representative of a low intensity surface fire, not a high intensity wildfire.

Repeatable field scale firespread experiments are extremely difficult to conduct due to cost, safety, and environmental variability. Only a few well characterized field-scale experiments exist (e.g., [29,30]). There are relatively few constraints on conducting numerical simulations of field scale firespread scenarios beyond computational cost. However, it is essential that the numerical simulation be validated, or evaluated, through comparison to controlled experiments (when possible) or field observations.

In the 2 m tall tree experiments conducted here, six trees had an average $M = 14\%$ and three trees had an average $M = 49\%$. For the 5 m tall trees the average $M = 26\%$. The trees were ignited using custom natural gas burners specifically designed for these experiments. Two burners, one for each tree height, were used. A photograph of the burner used for the 2 m tall trees is shown in Fig. 4. This ignitor was circular, with a diameter of 80 cm and a heat re-

lease rate of 30 kW. The ignitor was shut off after 10 s for the $M = 14\%$ trees and after 30 s for the $M = 49\%$ trees. The ignitor used for the 5 m tall trees was hexagonal with a span of 122 cm and a heat release rate of 130 kW. The ignitor was shut off after 30 s. The bottom area of each tree crown was pruned so that, as much as possible, the vertical distance between the burner and the crown base above it was 10 cm–20 cm for the 2 m tall trees and 30 cm for the 5 m tall trees. This was done for consistency of ignition. Both digital still photography and standard color video (standard 30 frames per second) were used to record the ignition and burning process. Additional experiments were conducted for firebrands generated from trees of each height. Results from this study are reported in a separate paper [20].

The mass of a tree was measured as it burned using two different load cells in order to resolve the disparate initial mass loading for the two tree heights considered. The voltage from the load cells was recorded using custom data processing software.

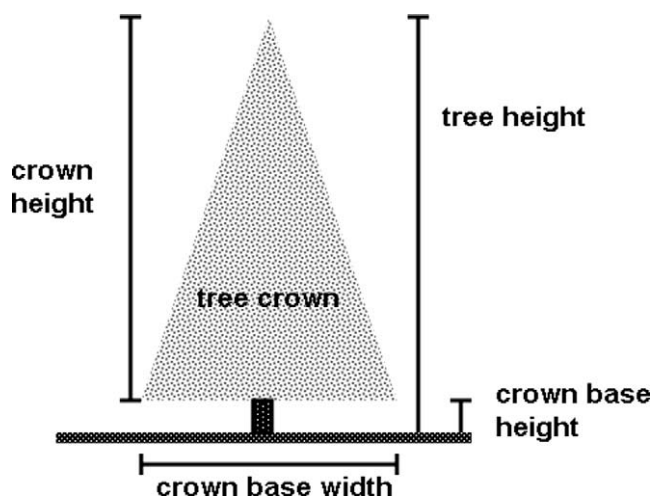


Fig. 3. Schematic showing different measures of a cone shaped tree. The width of the crown base was determined by measuring between the furthest extent of the branch tips in the bottom of the crown. Note that this may not correspond to the lowest branches. This was done in two orthogonal planes and the results averaged.



Fig. 4. A snapshot from a 2 m tall tree experiment showing the ignitor and load cell configuration.

Tables 1 and 2 list measured characteristics of the 2 m and 5 m tall trees, respectively, used in the experiments. Values for the vertical length of the crown, height to crown base, and total height (from ground to top of the crown) are listed. The crown base width is the average of the horizontal distance spanned by the lowest branches of the crown. The initial total mass is the mass of the entire tree (including moisture mass) just prior to ignition, the dry mass loss (Δm_{dry}) is obtained from the measured total mass loss, Δm_{total} , by:

$$\Delta m_{\text{dry}} = \frac{\Delta m_{\text{total}}}{1 + 0.01 M} \quad (2)$$

Note that Δm_{total} , which is not listed in Tables 1 and 2, includes mass loss from drying, the generation of fuel gases (i.e., pyrolysis), and char oxidation (smoldering). Determining Δm_{dry} from (2) assumes that the char mass is completely consumed, leaving ash of negligible mass. It is also assumed that the moisture of all consumed fuel equals the measured needle moisture. Comparisons of twig and needle moisture levels were consistent with the last assumption.

Table 1

Experimental data from 2 m tall Douglas fir trees (quantities in parentheses are the standard deviation). See Fig. 3 for an illustration of a tree crown and definitions of physical dimensions.

Test#	Height, m Crown, base, total	Crown base, m	Initial total mass, kg	Mass loss (dry, Δm_{dry}), kg	M (needles), %
1	2.1, 0.15, 2.25	1.7	13.6	2.7	48
2	2.1, 0.15, 2.25	1.8	15.0	3.1	50
3	2.0, 0.15, 2.15	1.8	11.9	3.2	49
4	2.1, 0.15, 2.25	1.7	8.1	3.4	20
5	1.9, 0.15, 2.05	1.7	8.3	4.0	17
6	1.9, 0.15, 2.05	1.7	9.5	4.8	14
7	1.8, 0.15, 1.95	1.5	11.2	3.7	10
8	1.8, 0.15, 1.95	1.7	11.3	3.9	12
9	1.9, 0.15, 2.05	1.4	9.5	3.8	10
Average	1.96 (0.1) Crown	1.7 (0.12)	T1-3: 13.5 (1.3) T4-9: 9.7 (1.3)	T1-3: 3.0 (0.2) T4-9: 3.9 (0.4)	T1-3: 49 (0.8) T4-9: 14 (3.7)

Table 2

Experimental data from 5 m tall Douglas fir trees (quantities in parentheses are the standard deviation). See Fig. 3 for an illustration of a tree crown and definitions of physical dimensions.

Test #	Tree height, m Crown, base, total	Crown base width, m	Initial total mass, kg	Δm_{dry} , kg	M (needles), %
2	4.2, 0.3, 4.5	3.4	67.2	21.4	31
3	4.2, 0.3, 4.5	3.0	53.7	18.1	23
4	4.3, 0.3, 4.6	2.3	52.9	17.0	23
Average	4.2 (0.05) Crown	2.9 (0.45)	57.9 (6.6)	18.8 (1.9)	26 (3.8)

Individual measured mass loss time histories and average mass loss rate time histories for the 2 m tall, $M = 49\%$, trees are plotted in Figs. 5a and b, respectively. The vertical lines in Fig. 5b are one standard deviation above and below the average mass burning rate. As seen in Fig. 5a, the mass loss curves for each experiment are shifted vertically so that they all start at zero mass. This allows more direct comparison since the initial mass does vary between experiments (see Table 1). The total mass loss varies from 4 to 5 kg, an average of 33% of the original tree mass. Very little roundwood burned and the foliage was completely consumed only in approximately the upper 2/3 of the crown, as can be seen in Fig. 6, and in the central region of the bottom 1/3 of the crown. Very few firebrands were produced as these require sufficient burning of the roundwood.

The total mass loss for the 2 m tall, $M = 14\%$, trees (Fig. 7a) varies from 4.1 kg to 5.5 kg for an average of 48% of the original tree mass. This total mass loss is about the same in the 2 m tall, $M = 49\%$, trees (although the mass loss was a smaller fraction of the original mass, 33%). The $M = 14\%$ trees burn over a shorter time interval since the fuel is drier and, therefore, pyrolyzes more readily. This is reflected in the behavior of the mass loss rates. The 2 m tall, $M = 14\%$, trees burn for approximately 20 s with a peak mass loss rate of 0.4 kg s^{-1} , as seen in Fig. 7b. The $M = 49\%$ cases burn about twice as long and have half the peak mass loss rate (about 0.2 kg s^{-1}). In the 2 m tall, $M = 14\%$, and 5 m tall cases, fuel moisture was low enough that all the foliage and most of the roundwood up to a diameter of 10 mm was consumed. An example of this can be seen in Fig. 8 which is at the end stage of flaming combustion. It can be seen that no foliage remains and a significant amount of roundwood is undergoing smoldering combustion.

The mass loss and average mass loss rate time histories for the 5 m tall trees are plotted in Fig. 9a and b, respectively. Approximately five times more mass is lost, 21 kg–28 kg or 40% of the total

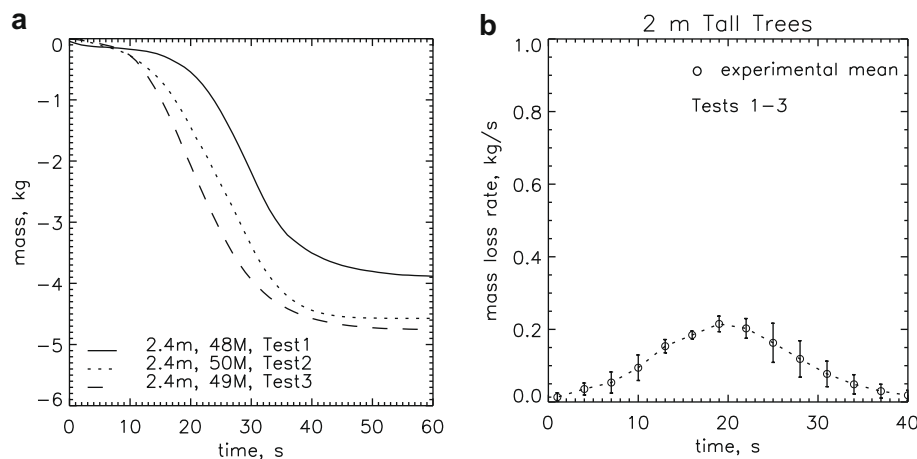


Fig. 5. Experimental results from burning the approximately 2 m tall trees with average moisture content of 49%. See Table 1 for more details. (a) Mass loss time history curves for each of the three experiments. (b) Average mass loss rate from data in (a). The vertical lines show one standard deviation above and below the average mass burning rate.

mass, compared to the 2 m tree cases. The trees burn for about 40 s and have a peak mass loss rate of $\dot{m}_{\max} = 2 \pm 0.2 \text{ kg s}^{-1}$, five times that of the drier 2 m tall trees $\dot{m}_{\max} = 0.4 \pm 0.1 \text{ kg s}^{-1}$. The variation in \dot{m}_{\max} is most likely due to differences in tree structure (such as intra-crown variation in bulk density). A first approximation to the peak heat release can be obtained by neglecting moisture mass loss: $\text{HRR}_{\max} = (1 - \chi_{\text{char}})\Delta h_c \dot{m}_{\max}$. This gives $\text{HRR}_{\max} = 5.2 \pm 1.3 \text{ MW}$ (2 m tree) and $26 \pm 2.6 \text{ MW}$ (5 m tree). The average of the measured HRR_{\max} is $3.7 \pm 0.9 \text{ MW}$ and $32 \pm 6 \text{ MW}$. The calorimetry system itself had a measurement uncertainty of $\pm 25\%$. The differences between the \dot{m}_{\max} based and the calorimetry measured HRR_{\max} are reasonable given the spread in the experimental results and the uncertainty in the calorimetry measurements.

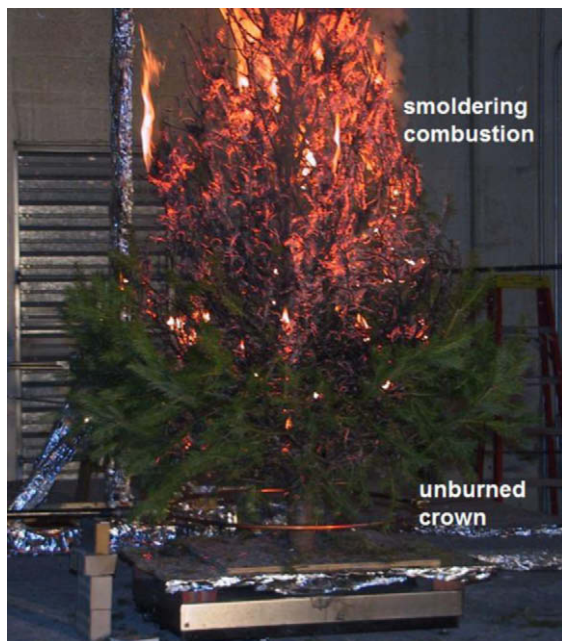


Fig. 6. Photograph of 2 m tall, 49% moisture, tree burn experiment at the end of the flaming stage. Corresponds to the dashed line result in Fig. 5a (i.e., Test 3 in Table 1) at approximately 40 s after ignition. A section of the outer perimeter (radius greater than the ignitor's) in approximately the bottom third of the tree crown is unburned due to the high moisture content of the vegetation. In burned areas, consumption is mostly limited to foliage. Essentially no firebrands are formed.

4. WFDS simulations of the experimental tree burns

Computer simulations of the three cases of Douglas fir burn-experiments were conducted: 2 m tall, 49% moisture content; 2 m tall, 14% moisture; and 5 m tall 26% moisture. Validation checks of the numerical simulation were made by comparing time histories of the predicted and measured mass loss rate and radiant heat flux. Mass loss rate is a fundamental quantity since it is the result of the coupled processes of heat generated by gas-phase combustion, convective and radiative transfer of this heat to the vegetation, and the resulting thermal degradation of the vegetation (mass loss) that can create additional fuel vapor for further combustion. Fig. 10 shows a series of snapshots from an experiment and characteristic simulation of a 2 m tall tree burn.

4.1. Model inputs

The numerical model requires a number of thermo-physical properties for the gas phase and the vegetative fuel. Required properties of the vegetative fuel are listed in Tables 1–3 and can be categorized as follows:

1. Crown properties

(a) *Geometry*: The computer model is capable of representing the shape of a tree crown at the resolution of a grid cell (ϕ (10) cm here). However, measuring the mass and size distribution of vegetation at this resolution would take significant effort. For simplicity, the crown is represented as a well defined shape such as a cone or cylinder. This requires measured or estimated values of the width and height of the crown base, the width of the crown top, and the total height of the tree. The average values of these physical dimensions are used to define the simulated 2 m and 5 m tall trees. For example, in the 2 m tall tree case (using dimensions of the six 2 m tall tree burns listed in Table 1) the average crown base width and height are 1.7 m and 0.15 m, respectively; and the average tree height is 2.1 m. These dimensions are sufficient to represent the tree as a cone. Overall, the 2 m trees were well represented by a cone. The 5 m trees were not as conical and simulations using both a cone and a cylinder were compared.

(b) *Bulk density*: The model equations require the bulk density of the dry (zero moisture) thermally-thin vegetation. While it is possible to bioassay tree crowns to obtain a spatially dependent bulk density, it would be at a significant time and labor cost. Also, the question of how to determine if the bioassayed trees are sufficiently representative of trees to be burned would need to

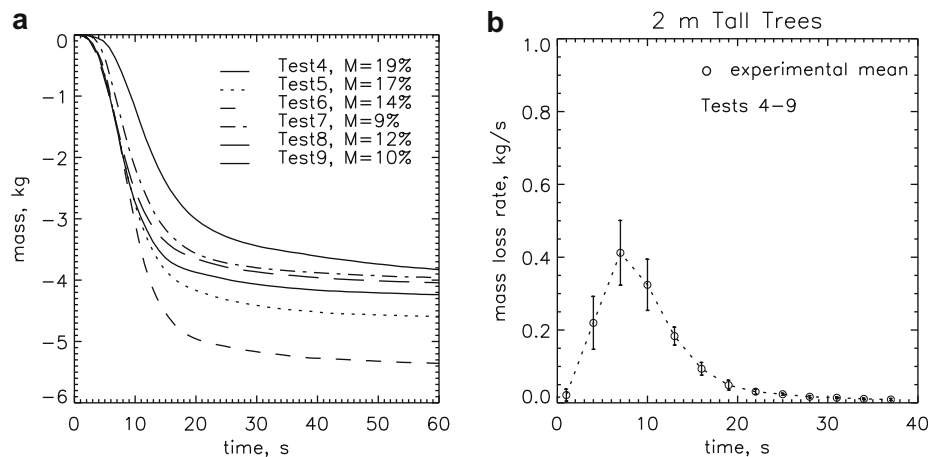


Fig. 7. Experimental results from burning the approximately 2 m tall trees with average moisture content of 14%. See Table 1 for more details. (a) Mass loss time history curves for each of the six experiments. (b) Average mass loss rate from data in (a). The vertical lines show one standard deviation above and below the average mass burning rate.

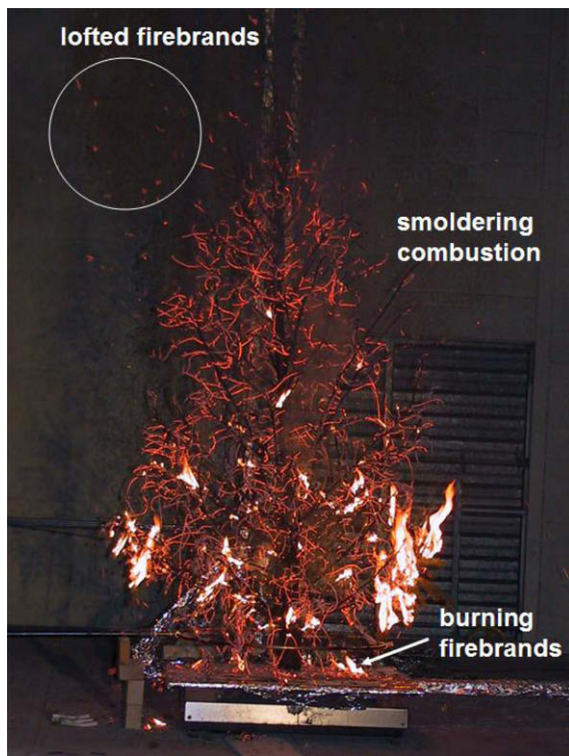


Fig. 8. Photograph of 2 m tall, 17% moisture, tree burn experiment at the end of the flaming stage. This experimental case is plotted with a dotted line in Fig. 7a (i.e., Test 5 in Table 1). The time at which the photo was taken is $t = 22$ s. Post-fire observations found that all the foliage and roundwood up to 10 mm in diameter was consumed. Firebrands from roundwood can be seen in the figure, many of which were drawn into the hood during the experiment. Other firebrands fell beneath the tree and burned via both flaming and smoldering combustion. Note that in the firebrand collection studies of Manzello [20], the hood was turned off to prevent loss of fire brands.

be addressed. Given the early stage of this study and limited resources, an approximation to the dry-fuel bulk density was obtained from the measured mass loss and limited tree biomass sampling (bioassays). It was observed that, for the 5 m trees and the drier 2 m trees all foliage and roundwood up to approximately 10 mm in diameter was consumed by the fire. It was assumed that the consumption of thermally-thin vegetation (i.e., foliage and roundwood ≤ 6 mm in diameter) dominated this mass loss. This

assumption was found to be consistent with measurements of the proportional distribution of biomass in the crown, as discussed below. In other words, for these relatively dry $M < 30\%$ trees, the fire pruned out the thermally-thin vegetation allowing an estimation of the thermally thin mass in the crown.

In order to determine the mass of vegetation in different size classes (up to 10 mm in diameter roundwood) two 2 m tall trees were sampled (one partially and the other fully). Mass measurements were obtained in the following four size classes: foliage, roundwood of diameter ≤ 3 mm, roundwood 3–6 mm in diameter, and roundwood 6–10 mm in diameter. The distribution of dry mass in these size classes was approximately 64%, 11%, 10%, and 15%, respectively. A similar distribution of mass was found in the 5 m tall trees from sampling five branches of one tree (sampling an entire 5 m tree was too costly). The mass distribution for the 5 m tall tree were: 60%, 17%, 12%, and 11%. Thus, averaging the 2 m and 5 m cases, the 6–10 mm diameter roundwood contributes only 13% to the measured burned mass (assuming that mass loss in roundwood greater than 10 mm diameter is negligible).

In the $M < 30\%$ trees an estimate for the bulk density of the dry thermally-thin dry fuels can be obtained from the measured loss of dry mass, $\Delta m_{\text{exp,dry}}$, and an estimated volume of the tree crown, $\rho_{\text{bv}} = \Delta m_{\text{exp,dry}} / V_{\text{crown}}$. This global bulk density value can be broken up into bulk densities for the different size classes based on the mass distribution values given above. Values of ρ_{bv} are listed in Table 3.

The determination of the bulk density of the thermally thin fuels in the higher moisture case, $M = 49\%$, could not be as directly obtained from the measured mass loss because not all the thermally thin fuels in the crown were consumed. This is discussed in more detail in Section 4.2.2. In all cases the vegetation is assumed to be distributed uniformly throughout the tree crown so that the bulk density is spatially independent.

(c) **Packing ratio:** The packing ratio, $\beta = \rho_{\text{bv}} / \rho_e$, is an important parameter in the drag and radiation heat transfer (see Appendix). Its value depends on the bulk property of ρ_{bv} (discussed above) and the fuel element property of ρ_e (discussed below).

2. **Fuel element properties** The numerical model requires the following properties of the fuel elements (also see Table 3).

- (a) **Density:** A value of $\rho_e = 514 \text{ kg m}^{-3}$ was used for the fuel element density [31].
- (b) **Initial temperature:** The initial temperature of the fuel elements was assumed to be the same as the measured air temperature or prescribed by the user.

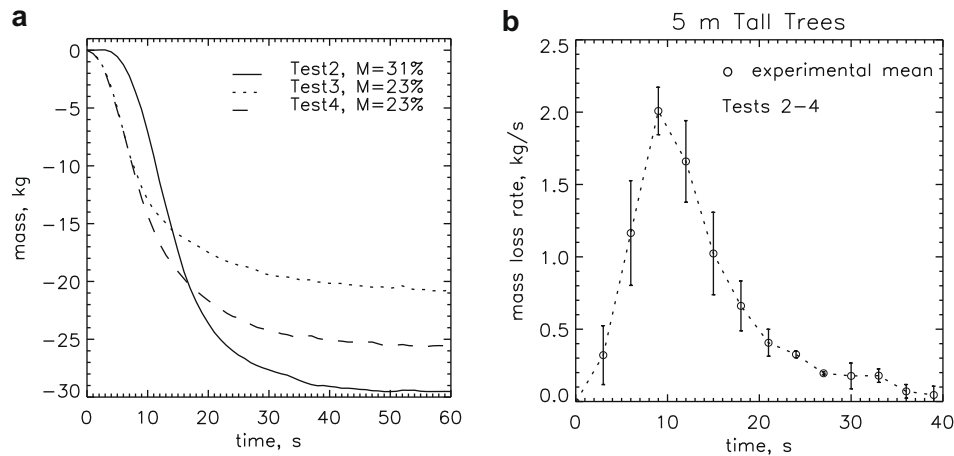


Fig. 9. Experimental results from burning the approximately 5 m tall trees with average moisture content of 26%. See Table 2 for more details. (a) Mass loss time history curves for each of the three experiments. (b) Average mass loss rate from data in (a). The vertical lines show one standard deviation above and below the average mass burning rate.

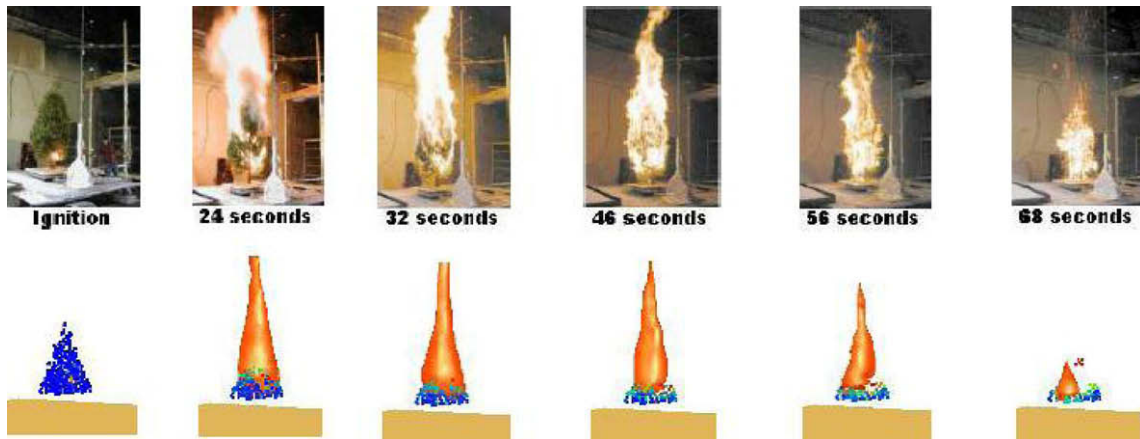


Fig. 10. Snapshots showing the characteristic stages of burning of a 2.4 m tall Douglas fir. Both experiments and simulations are shown. Photographs of the tree burning in NIST's Large Fire Laboratory are along the top row. The bottom row shows a WFDS computer simulation of the burning tree as rendered by Smokeview (NIST's visualization tool). The vegetative fuel is represented by point which are colored by temperature (blue is ambient, red is pyrolysis temperature). A heat release rate surface is displayed in orange (approximates the location of the flame). This tree is from an earlier set of scoping experiments and has a larger bulk density ($\rho_{bv} = 8 \text{ kg m}^{-3}$; $M = 24\%$) than the final set of 2 m tall trees in Table 1. This resulted in a longer burn time.

- (c) *Moisture*: The fuel element moisture was defined to be the average of moisture (see Eq. (1)) measured from the trees for a given case. These measurements were made at a number of locations in the thermally thin fuels within the tree crowns.
- (d) *Char fraction*: Susott measured the char fraction for Douglas fir foliage, stems, and wood [32]. The average of these measurements, $\chi_{e, \text{char}} = 0.26$, was used here.
- (e) *Specific heat*: The relation for the specific heat of dry virgin Douglas fir reported by Parker [33] was used (see Table 3).
- (f) *Surface-to-volume ratio*: The surface to volume ratio ($\sigma = 3940 \text{ m}^{-1}$ with standard deviation of 366 m^{-1}) of the needles was obtained by averaging measured dimensions (length, width, and thickness) of 30 needles with calipers (accurate to $\pm 0.0125 \text{ mm}$). The needle shapes were closer to flat strips than cylinders.

Most model inputs for the gas phase are discussed in Appendix A. The heat of combustion, $\Delta h_c = 17,700 \text{ kJ kg}^{-1}$, is the heat released per kg of gaseous fuel (not per kg of solid fuel). It is derived from the char fraction and the average heat of combustion of vol-

atiles measured from Douglas fir wood and foliage [32]. Note that in [32] the reported the heat of combustion is of volatiles per kg of the virgin fuel, $\Delta h_{c, \text{volatiles}}$, so that

$$\Delta h_c = \frac{\Delta h_{c, \text{volatiles}}}{1 - \chi_{\text{char}}}.$$

The char fraction is

$$\chi_{\text{char}} = \frac{m_{e, \text{char}}}{m_{e, v}}.$$

The experimental ignition procedure at the bottom of the tree crown was approximated by placing a ring of hot spots within the base of the simulated crown. The location and diameter of these rings matched that of the flame from the experimental burners (within the constraints of grid resolution). The simulated rings were held hot for the same duration that the ignitors were flaming in the experiments (10 s and 30 s for the 2 m tall trees with $M = 14\%$ and 49% , respectively; 30 s for the 5 m tall tree). This simulated ignitor induced a buoyant flow of hot air on the vegetation with an average temperature of 800 C.

Table 3

Thermo-physical properties required in model. A ndash (–) indicates that the property was not measured. Values of these unknown properties in the simulation were either assumed or representative values were obtained from the literature sources cited.

	Symbol, units	Value used	2 m Trees	5 m Tree	Comments
Gas phase	Δh_c , kJ kg ^{−1}	17,700	–	–	Douglas fir [32] ^a , Section 4.1
	χ_r	0.35	–	–	Wood cribs [34] ^a
	χ_s	0.02	–	–	Douglas fir [35] ^a
	$T_{g,a}$, C	Measured	20	28	
Solid phase	σ , m ^{−1}	3940	–	–	Measured
	χ_{char}	0.26	–	–	Douglas fir [32] ^a
	$c_{p,v}$, kJ kg ^{−1} C ^{−1}	Varies with T_s	–	–	=1.11 + 0.0037 T_s [33]
	$c_{p,m}$, kJ kg ^{−1} C ^{−1}	4.22	–	–	[36]
	ρ_e , kg m ^{−3}	514	–	–	Douglas fir [31]
	ρ_{bv} , kg m ^{−3}	Derived	2.63	2.03	All veg ≤10 mm
			3.95	–	Cone crown, $M = 14\%$
			–	1.76	Cylinder crown
	$\beta_e = \rho_{bv}/\rho_e$	Derived	0.005	0.004	$M = 14\%$ 2 m tree
			0.008	–	$M = 49\%$ 2 m tree
			–	–	See discussion in Section A.6
	$T_{e,a}$, C	$T_{g,a}$	–	–	Assumed

^a Representative value from the range of values found in the cited reference.

4.2. Model results and discussion

The sensitivity of the model predictions of mass loss rate and radiant heat flux on both grid resolution and computational domain size was tested. The computational domains of the “production” runs were 3 m × 3 m × 6 m (in x,y,z directions with z vertical) for the 2 m tall trees and 6 m × 6 m × 9 m for the 5 m tall trees. Mass loss rates and heat fluxes from simulations with twice the edge length (eight times the volume) were within 15% of the production run simulations. The grid resolutions were uniform with 7.5 cm cells for the 2 m tall trees and 10 cm for the 5 m tall trees in the production runs. Simulations with half the grid size had peak mass loss rates that were 15% lower. Future work will better identify the source and sensitivities of these variations in the model results which can be due to our representation of the vegetation and/or our numerical and physical modeling approaches.

The simulations were run on four 3.1 GHz processors. The 2 m tall tree runs required 250 MB of memory and 23 net cpu minutes for 30 s of simulated time (4300 time steps). The 5 m tall tree runs required 440 MB memory and 280 net cpu minutes for 35 s of simulated time (15,300 time steps).

As discussed in Section 4.1 an estimate of the bulk density of the thermally-thin vegetation can be obtained from the measured dry mass loss in the $M < 30\%$ tree burns. This was done in two ways: the thermally-thin vegetation was either (1) all foliage or (2) distributed in the size classes discussed in Section 4.1. The first method has the advantage of ease of implementation, only the total mass of the dry thermally-thin vegetation is needed, which can potentially be related via a rule of thumb or an allometric equation to general tree characteristics. The second method more realistically accounts for the distribution of mass in size classes, but the mass distribution used here may not be generally applicable.

As stated above, post-burn observations of the experiments determined that the foliage and smaller roundwood (<10 mm) for the drier 2 m tall trees and the 5 m tall trees were removed from the tree during burning. This process was not directly mod-

eled but can affect heat transfer within the crown by altering the fluid flow (via drag) and radiant heat fluxes (via changes in radiation absorption/emission). In order to assess the importance of this affect on model predictions the removal of a pyrolyzed fuel element was handled in two ways. In the first approach, once pyrolysis is complete, leaving only char, a fuel element remains for the duration of the simulation as a source of drag, thermal mass, and radiative absorbtion/emission. In this case, the equation for the fuel element temperature (Eq. (25) in the Appendix) is solved without the thermal degradation terms. Both σ and β retain their original values during the post-pyrolysis phase since the charred vegetation is assumed to have the shape and size of the virgin fuel. In the second approach, once the virgin fuel is fully pyrolyzed it is removed from the computational domain.

4.2.1. 2 m Tall, $M = 14\%$ trees

In order to gain an understanding of the global results, such as the average mass loss rate obtained by weighing the burning tree, we first present some more local results for the case of a tree crown composed of foliage only. Time histories of the fuel elements located in a grid cell 38 cm from the top of the tree crown on the vertical centerline are plotted in Fig. 11. The net bulk density (dry fuel plus moisture mass per unit volume) and the temperature of the fuel element and gas phase are plotted in Fig. 11a when keeping pyrolyzed fuel elements and in Fig. 11b when removing pyrolyzed fuel elements. The general character of the time histories is similar for both the foliage kept and foliage removed cases. After approximately 6 s the fuel element temperature (solid line) rises due to immersion in hot gases (dotted line). Drying begins at $t \approx 8$ s when $T_e = 100^\circ\text{C}$. Drying lasts approximately 3 s after which T_e rises rapidly and volatilization begins at $t \approx 12$ s. The pyrolysis is complete by $t \approx 22$ s when the charred foliage is kept and earlier, by $t \approx 20$ s, when the charred foliage is removed.

In both cases (pyrolyzed fuel elements kept or removed) pyrolysis is completed before the flame zone reaches the fuel element. However, from the gas phase temperature time history it is clear that in Fig. 11b the fuel elements are at the edge of the flame zone as pyrolysis ends at $t \approx 20$ s. For the case in which the pyrolyzed fuel elements are kept, the flame zone (the $T = 700^\circ\text{C}$ peak in Fig. 11a) does not reach the fuel elements until $t \approx 27$ s, 5 s after pyrolysis is complete. The proximity of the flame zone results in larger heat fluxes on fuel elements when the pyrolyzed fuel elements are removed. This can be seen from the histories of the divergence of the conductive and radiative fluxes on the fuel elements, in Fig. 11c and d. In both figures, radiation dominates convective heat flux. However, during the last half of pyrolysis in Fig. 11d ($16\text{s} \leq t \leq 20\text{s}$; pyrolyzed fuel elements removed) the radiative contribution rises rapidly due to the approach of the flame zone.

Fig. 12 shows the average mass loss rate from the 2 m tall, $M = 14\%$, tree burning experiments (circles) and from WFDS simulations (lines). The mass loss rate is a fundamental quantity that results from the coupled fire/fuel interaction as the fire spreads through the vegetation. The experimental data is plotted as circles for the average mass loss rate, with vertical bars denoting the range of one standard deviation above and below the average value. In Fig. 12a the tree crown is represented solely by foliage (the case with pyrolyzed foliage kept is the solid line; pyrolyzed foliage removed is the dashed line). The behavior of the mass loss rate in Fig. 12a is clearly consistent with the local time histories discussed above in Fig. 11: the case with pyrolyzed fuel elements removed has a larger mass loss rate. The duration of burning in both the simulation cases in Fig. 12a is similar to the experiments but the peak mass loss rate occurs later and is lower in magnitude than the experiments (25% lower for the case of removing pyrolyzed fuel elements).

In Fig. 12b the average mass loss rate from the experiments and from the simulation with the tree crown represented by four types of vegetation is plotted. The four vegetation types and their approximate percentage of the total simulated crown mass are: foliage (64%), and three roundwood types with diameters <3 mm (11%), 3 mm–6 mm (10%), 6 mm–10 mm (15%). Thermal degrada-

tion of the thermally-thick roundwood of size 6 mm–10 mm is not modeled; this vegetation type is present in the simulation as a source of drag and radiative absorption. As discussed in Section 4.1, the dry bulk density of the tree crown is obtained from the measured mass loss and the volume of the cone approximating the crown, $\rho_b = 2.63 \text{ kg m}^{-3}$. In the case with four vegetation types

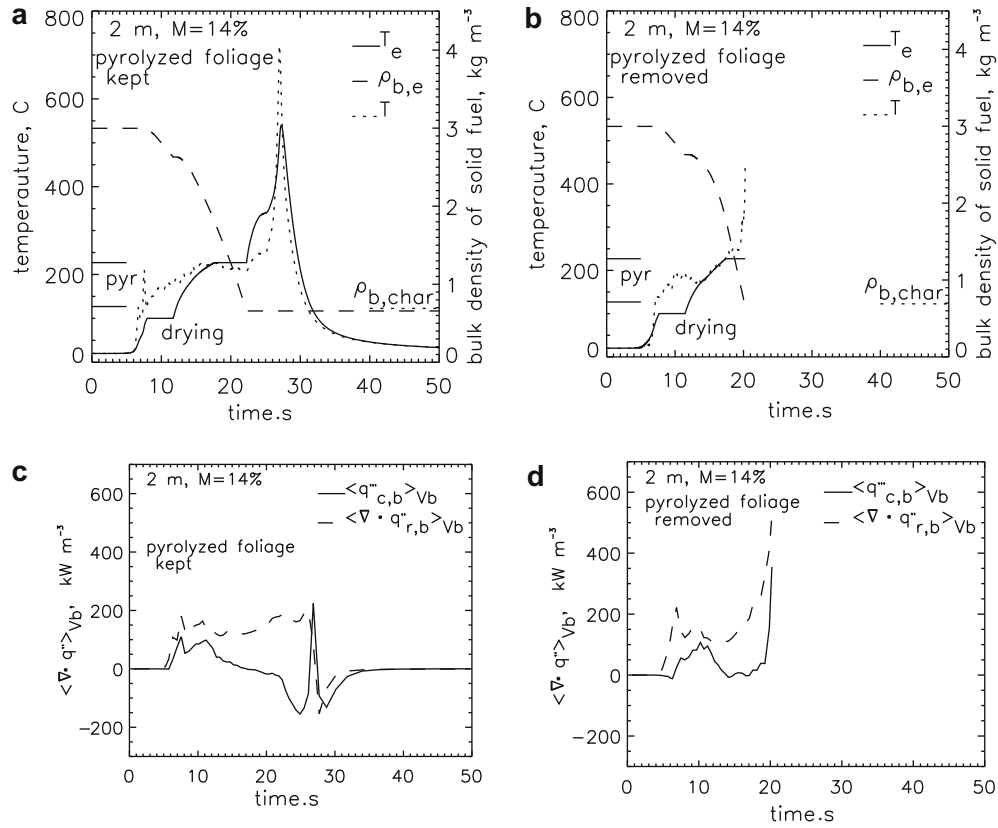


Fig. 11. Time histories of various fuel element quantities in a grid cell located along the tree's vertical centerline, 38 cm from the top of the tree. The cases of pyrolyzed vegetation kept (a,c) and removed (c,d) are shown. The top row has time histories of fuel element temperature (solid line), gas phase temperature (dotted line), and net bulk density (dashed line). Note that the bulk density minimum equals the char density. The bottom row contains time histories of the divergence of the convective and radiative heat fluxes. Note these terms are in the fuel element temperature Eq. (25).

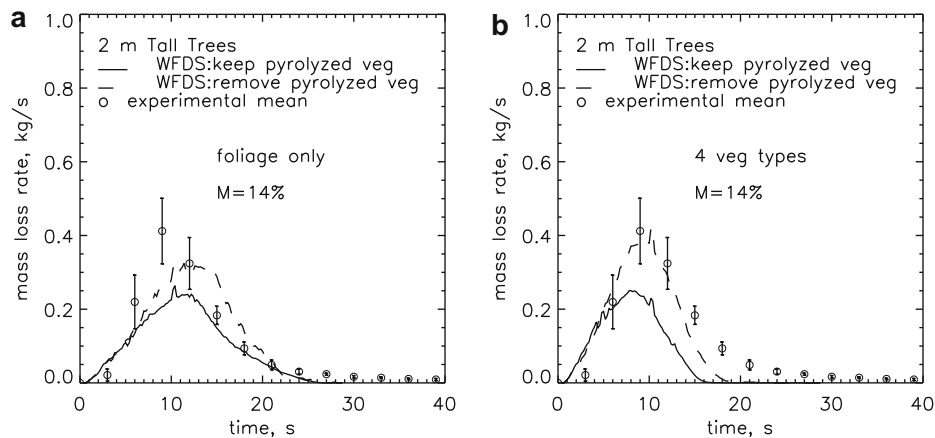


Fig. 12. Mass loss rate versus time for the 2 m tall, $M = 14\%$, trees from the experiments and the simulations. The average mass loss rate from the six experimental burns are circles with vertical lines showing one standard deviation above and below the average. Solid and dashed lines are WFDS results and distinguish between two methods of handling a fuel element after the virgin fuel has burned off leaving only char. For the solid line case the fuel element is kept as a source of drag, thermal mass, and radiative absorption/emission. For the dashed line case the fuel element is removed from the simulation. Char oxidation is not modeled in either case. (a) Tree crown is assumed to consist solely of foliage. (b) Tree crown consists of vegetation (fuel elements) of four different sizes, as determined from bioassay measurements.

the portioning of the mass into each type, based on bioassay measurements of the trees (see Section 4.1), gives: $\rho_{be} = 1.68 \text{ kg m}^{-3}$ (foliage), 0.29 kg m^{-3} (<3 mm roundwood), 0.26 kg m^{-3} (3 mm–6 mm), and 0.39 kg m^{-3} (6 mm–10 mm).

The results with four vegetation types in Fig. 12 are consistent with the earlier results: removing pyrolyzed fuel elements increases the mass loss rate and gives results closer to the measured values. Splitting the fine fuels among three size classes lowers their bulk density, compared to the single size foliage only case. This effectively reduces the overall drag and the thermal inertia in the crown, allowing ignition and firespread to occur more readily. The peak mass loss rate occurs earlier and is in good agreement with the experiments results when pyrolyzed fuel elements are removed. Note, these results are encouraging but more work is

needed to test and refine the drag model and to determine the influence of bulk density, especially at lower values which are more representative of natural Douglas firs.

Radiation can play a central role in WUI firespread by preheating fuels ahead of the fire front, thereby aiding piloted ignition from direct flame contact or, potentially, from firebrands generated by burning vegetation and/or structures. Fig. 13 shows the time history of the measured total heat flux in the experiment (circles) and the incident radiant flux in WFDS (lines). Heat flux locations are at two different horizontal distances from the center of the tree ($x = 2 \text{ m}$ or 3 m) each with four heights above the base of the tree trunk ($z = 0.2 \text{ m}$, 1.2 m , 2.3 m , 3.4 m , 4.5 m). All flux gauges were manufactured by the Medtherm Corporation and all ten total flux gauges were water cooled using cold tap water. The five gauges lo-

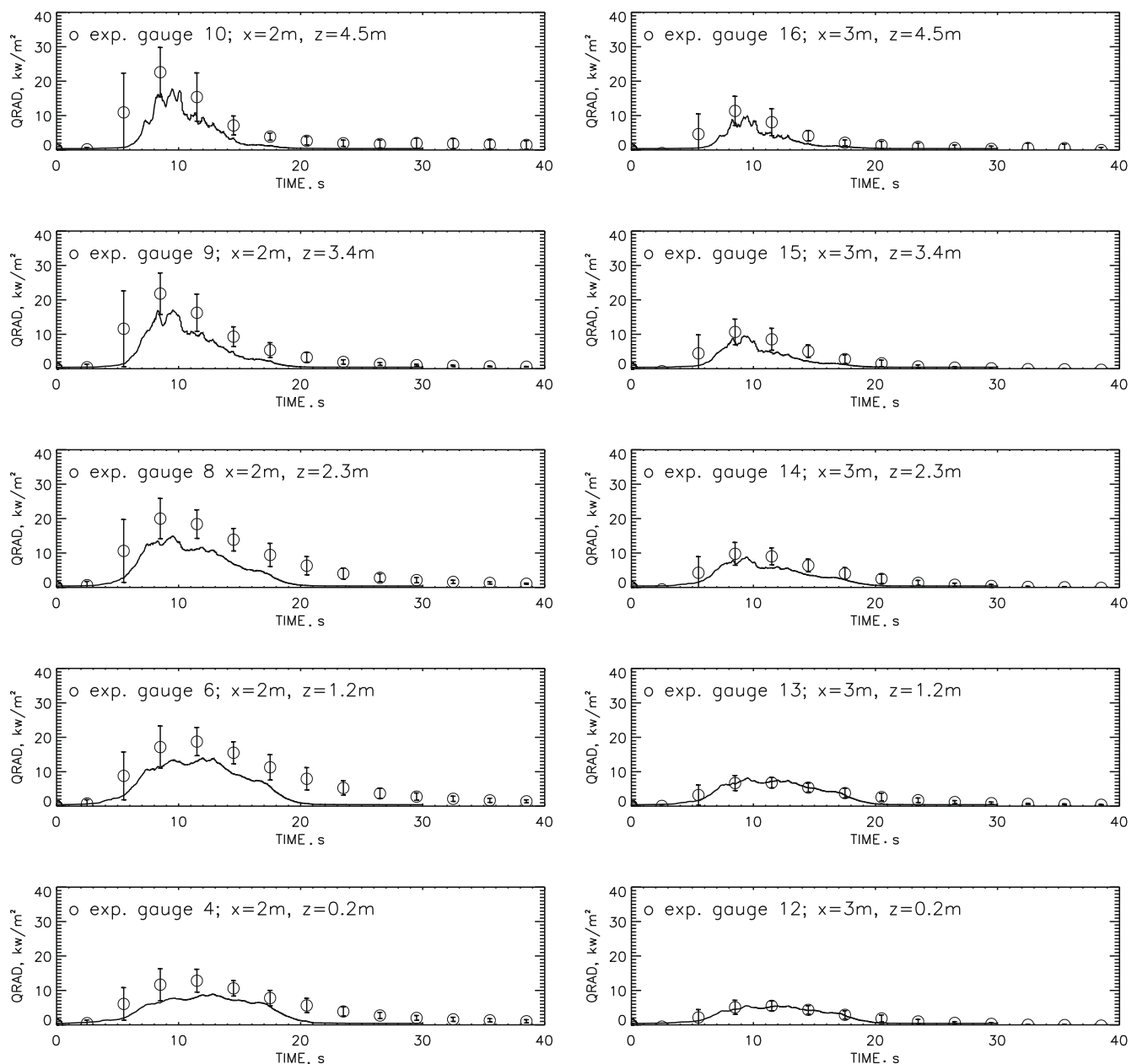


Fig. 13. Time histories of the incident radiant heat flux (kW m^{-2}) for the 2 m tall, $M = 14\%$ experiments and WFDS simulation. The average total heat flux from the six experimental burns are circles with vertical lines showing one standard deviation above and below the average. WFDS results are solid lines; the tree is modeled with four vegetation types with pyrolyzed vegetation removed (same case as the dashed line in Fig. 12b). The radiant flux was measured by total heat flux gauges facing the tree at five different heights and two horizontal distances from the center of the tree. The left column of figures correspond to gauges located a horizontal distance of $x = 2 \text{ m}$ and vertical locations of (from bottom to top of the figure) $z = 0.2 \text{ m}$, 1.2 m , 2.3 m , 3.4 m , 4.5 m . For the right column of figures $x = 3 \text{ m}$ and same heights as left column.

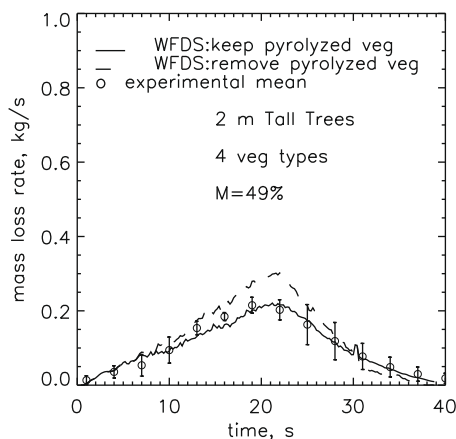


Fig. 14. Measured (circles) and predicted (solid and dashed lines) time histories of the mass loss rate versus time for the 2 m tall, $M = 49\%$, trees. Circles show the mean mass loss rate from the three experiments; vertical lines on circles denote one standard deviation above and below the mean. Fuel elements of four sizes, based on bioassays and observation (see discussion in Section 4.2.2) represent the vegetation. The solid line denotes the simulation case in which pyrolyzed vegetation is retained; the dashed line is the case of pyrolyzed vegetation removed.

cated 2 m from the tree trunk were factory calibrated up to 150 kW m^{-2} using cold water. The second set of five flux gauges, located 3 m from the tree trunk, were also cold water factory calibrated to 100 kW m^{-2} . The two standard deviation uncertainty of the flux gauges is estimated at $\pm 3 \text{ kW m}^{-2}$. By incident radiant flux in WFDS we mean the radiant flux in the gas phase.

The simulated incident radiation flux can be legitimately compared to the measured total flux because the contribution of the convective heat flux is negligible, based on temperature at the gauge location ($\leq 8^\circ\text{C}$ above ambient in the simulations). The face of experimental flux gauges are oriented to be parallel to the tree trunk, this orientation is accounted for in the computation of the incident radiant flux. The simulated crown is represented by four fuel element types with pyrolyzed fuel elements removed (solid lines; this is the same WFDS case plotted as a dashed line in Fig. 12 b). The maximum heat flux increases and occurs earlier as the height of the measurement increases. This peak flux behavior is due to the fire occupying a larger view angle at the higher measurement locations. The time shift occurs because the duration of

the burn is longer at lower heights where there is more fuel loading (see Fig. 2). These trends are reproduced in WFDS. As with the mass loss rate predictions (Fig. 12b), WFDS under predicts the duration of burning. In other respects WFDS gives reasonable predictions of the radiant heat flux.

4.2.2. 2 m Tall, $M = 49\%$ trees

Determining the fuel mass loading for the $M = 49\%$, 2 m tall, trees is more problematic than for the $M = 14\%$, 2 m tall trees. As seen in the photos from the experiments, unlike the drier trees (see Fig. 8), foliage and roundwood less than 10 mm in diameter are not completely consumed throughout the crown in the $M = 49\%$ tree burns (see Fig. 6). For this reason, it was not possible to use the total dry mass loss as a first approximation to the mass of vegetation in the tree crown that is 10 mm in diameter or smaller. However, from post-burn observations of the $M = 49\%$ burns, it was estimated that the burned region occupied the entire upper 2/3 of the crown and a cylindrical region in the bottom 1/3 of the crown with a diameter approximately equal to the burner diameter. In this burn region, to a first approximation, the mass loss was predominately from completely consumed foliage, relatively little roundwood was consumed. From the volume of the burned region, the volume of the entire crown, the measured mass loss, and the assumption that only foliage was consumed, we estimate the mass of foliage to be 3.75 kg. This allows for an approximate determination of the mass of vegetation in the crown that is less than 10 mm in diameter (since from bioassays 64% of this crown mass is foliage). This gives 5.86 kg. As with the $M = 14\%$ case, this mass is portioned into four size types in WFDS.

Fig. 14 shows the mass loss rate from the WFDS simulations. In these simulations, the shape of the tree crown was approximated by a cone. As in the $M = 14\%$ case of Fig. 12, the solid and dashed lines correspond to the case of keeping and removing, respectively, the fuel elements after they are completely pyrolyzed. Both cases give good predictions of the burn duration and the location of the mass loss rate peak. The magnitude of the peak mass loss rate is well predicted when pyrolyzed fuel elements are kept and over predicted by approximately 35% when the pyrolyzed fuel elements are removed. It is important to note that the method for obtaining the initial vegetative mass (as described in the preceding paragraph) is an approximation. Further work is underway to develop better measures of mass in the tree crown. This will support more rigorous testing of WFDS.

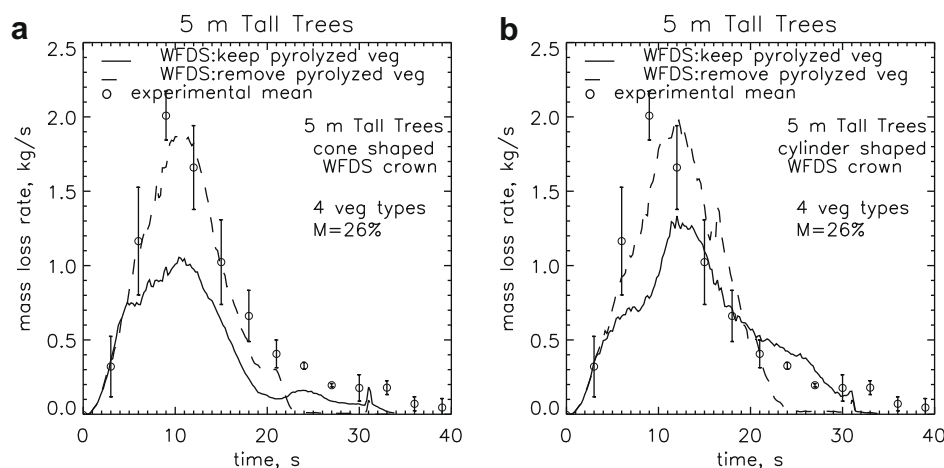


Fig. 15. Time histories of mass loss rate from the experiments (circles) and simulations (solid and dashed lines) for the 5 m tall, $M = 26\%$, trees. Circles show the average mass loss rate from the six experimental burns, with vertical lines showing one standard deviation above and below the average. Solid lines denote the simulation case in which pyrolyzed vegetation is retained; the dashed lines are the case of pyrolyzed vegetation removed. (a) Tree crown shape is approximated by a cone. (b) Tree crown shape is approximated by a cylinder.

4.2.3. 5 m Tall, $M = 26\%$ trees

Time histories of the mass loss rate for the 5 m tall trees are shown in Fig. 15. The shape of the tree crown is approximated by a cone in Fig. 15a and a cylinder in Fig. 15b. The crown vegetation is represented by four size types of fuel elements, in the same manner used above for the 2 m tall trees. The peak mass loss rate occurs near $t = 10$ s, as in the 2 m tall trees. The simulated peak is delayed in the simulations (by less than 3 s) compared to the measured peak. Similar to the drier 2 m tall tree case, the tail of the burn is not well predicted. This is consistent with the absence of char oxidation and burning of the 6 mm–10 mm diameter roundwood in the model. Also, as was discussed for the drier 2 m tall trees, removing the pyrolyzed fuel elements results in significantly high-

er peak mass loss rates, due to higher heat fluxes on the fuel elements, and predictions that are closer to the measurements (within 5% in Fig. 15).

Total heat flux time histories are shown in Fig. 16 at the same measurement locations used in the 2 m tall tree, $M = 14\%$, tree shown previously in Fig. 13. Note the difference in scales for the heat flux axis compared to the 2 m tall tree case figure. The maximum measured average incident heat fluxes in the 5 m tall tree ($\approx 55 \text{ kW m}^{-2}$) are approximately twice those of the 2 m tall tree ($\approx 25 \text{ kW m}^{-2}$). The simulated peak fluxes are also approximately twice those of the 2 m tall tree simulations. The under prediction of the burn duration results in an under prediction of the flux during the latter part of the burn.

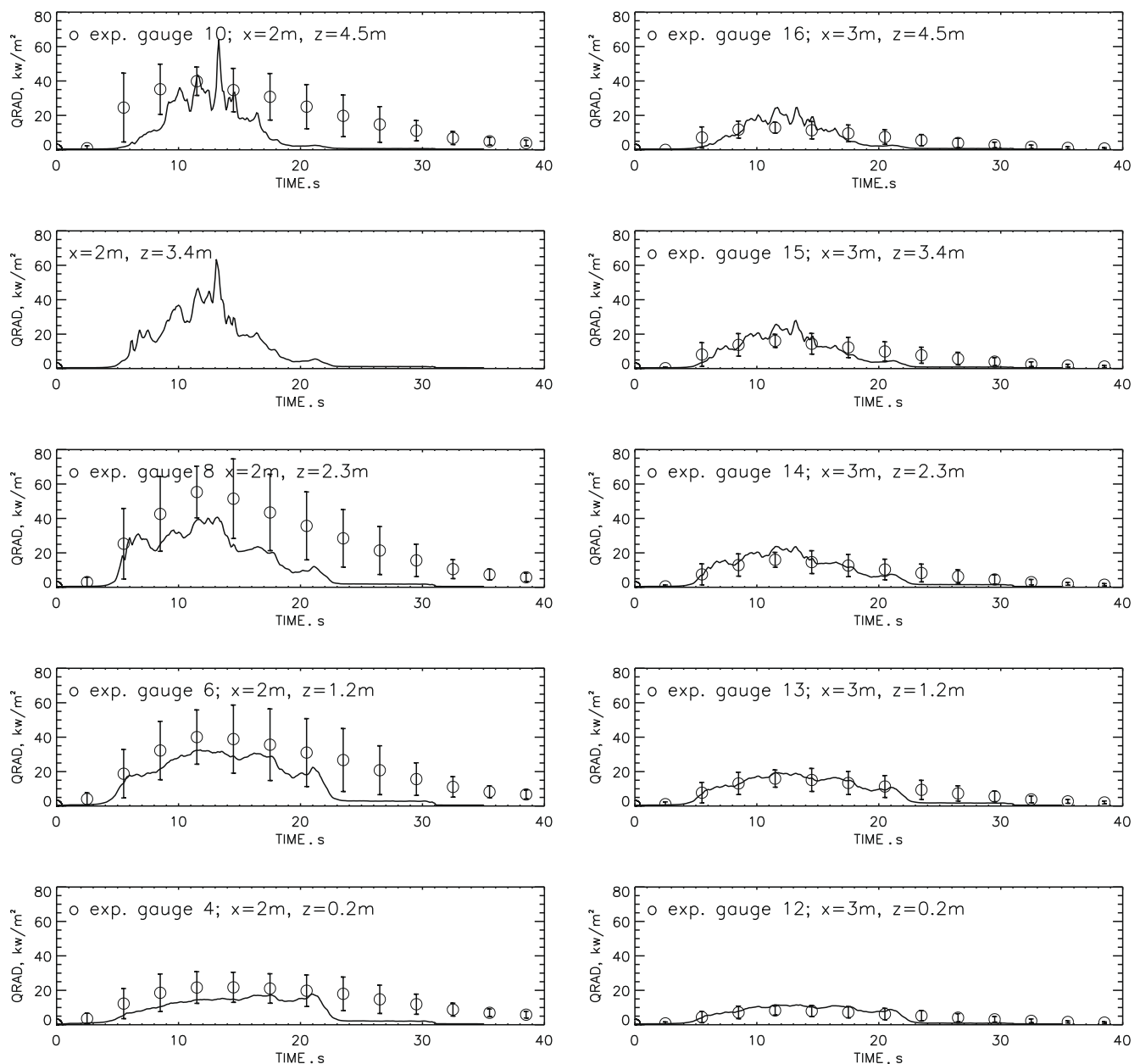


Fig. 16. Time histories of the incident radiant heat flux (kW m^{-2}) for the 5 m tall, $M = 26\%$ experiments and WFDS simulation. The average total heat flux from the six experimental burns are circles with vertical lines showing one standard deviation above and below the average. WFDS results are solid lines; the tree crown is modeled as cone shaped with four vegetation types with pyrolyzed vegetation removed (same case as the dashed line in Fig. 15b). The radiant flux was measured by total heat flux gauges facing the tree at five different heights and two horizontal distances from the center of the tree (same locations as for the 2 m tall trees). The left column of figures correspond to gauges located a horizontal distance of $x = 2$ m and vertical locations of (from bottom to top of the figure) $z = 0.2$ m, 1.2 m, 2.3 m, 3.4 m, 4.5 m. For the right column of figures $x = 3$ m and the same heights. The measured heat flux data for $x = 2$ m and $z = 3.4$ m was corrupted and is not included.

5. Summary and conclusions

A numerical modeling approach applicable to the simulation of fire spread through raised vegetation was developed and tested against measurements from experiments of individual tree burns. Model predictions of mass loss rate and radiative heat flux compare reasonably well to measurements. The laboratory conditions are representative of field conditions of tree crown ignition from a surface fire spreading through grass or a pine needle bed in no ambient wind. In such transition conditions, as opposed to ignition from a fully developed crown fire (with much higher incident heat fluxes), the tree burning behavior is expected to be sensitive to characteristics of the tree crown vegetation. This was observed in the results: burning behavior depended significantly on moisture and the method of representing the bulk density.

In the experimental burns, vegetation is removed from the tree to form firebrands (especially the drier, $M < 30\%$, cases). The mechanics of firebrand generation were not directly modeled. However, the influence of this process on the mass loss rate was bounded by either removing or retaining fuel elements once they reached a fully pyrolyzed state. Note that this significantly alters the drag and radiant absorption characteristics of the tree crown. In the drier tree cases, removing the fully pyrolyzed vegetation gave better predictions. Determining whether this method of approximating the mechanism of firebrand generation has general application requires further research.

Although the bulk density of the farm grown trees used here may be representative of residential vegetation, it is not representative, in general, of trees growing naturally on the landscape. It is expected that in a natural setting the bulk density and its spatial distribution will be less uniform. While forest stands may, to a first approximation, be modeled as uniformly distributed vegetation (if, for example, tree crowns are sufficiently close to each other) this ignores the important influence on firespread of patchy or inhomogeneous fuels. This is an important issue that needs to be addressed to improve our understanding of fire behavior in both wildland fuels that have been treated and in the discontinuous and heterogeneous fuels of the wildland–urban interface.

Future work on WFDS will focus on validation for fuels that are more representative of, for example, the bulk density and spatial distribution of naturally occurring vegetation in forest stands and landscapes near WUI communities. In conjunction with wind tunnel experiments, testing and refinement of the drag and convective heat transfer model will be carried out. The influence of wind and different thermal degradation models that include, for example, char oxidation will also be investigated. However, the model in its present form could feasibly be used to evaluate the radiant fluxes on structures, and other WUI fuels, due to burning ornamental trees ignited by surface fires. Ongoing experimental work on the transport and ignition potential of firebrands will also be used to extend and validate the model.

Acknowledgments

The authors would like to thank Dr. Ron Rehm of NIST (retired) for many fruitful discussions. The tremendous effort and contribution of the other developers of NIST's Fire Dynamics Simulator is also acknowledged: Kevin McGrattan (NIST), Simo Hostikka, (VTT Technical Research Center of Finland), Jason Floyd (Hughes Associates, Inc.), and Howard Baum (NIST – retired). Experiments in the Large Fire Laboratory were conducted with the excellent support of Mr. Loren DeLauter, Mr. Edward Hnetkovsky, and Mr. Jack Lee (deceased). Partial funding for this work received by the The Joint Fire Sciences Program under Project JFSP 07-1-5-08 and the US Forest Service, which are gratefully acknowledged.

Appendix A. Details of the modeling approach

A.1. Subgrid vegetation

We denote the volume over which a bulk property of the thermally-thin vegetation is determined as V_b , which is also the volume of a computational grid cell (see Fig. 1). As shown in Fig. 1(b,II), the vegetation in the tree crown is idealized as subgrid fuel elements uniformly distributed throughout V_b . The volume of a thermally thin fuel element k , of type e , is $V_{e,k} \ll V_b$. Different vegetation types can be distinguished by size or geometry (e.g., foliage versus roundwood) or some other relevant physical property (e.g., moisture content). Throughout the remainder of this paper the subscript e is suppressed, except when necessary for clarification. It is further assumed that $\sum_e \sum_k V_{e,k} \ll V_g$ where V_g is the volume occupied by the gas in V_b . Thus, thermally-thin vegetation is approximated as point sources of mass, drag, heat release, and radiative absorption and emission. Their effect on the gas-phase conservation laws comes via “bulk” source terms determined by summing the contributions of all the fuel elements in V_b . The formalism for deriving the bulk source terms used in the model equations is similar in concept to the filtered density function (FDF) approach introduced by Pope [37].

Although the derivation of the modeling equations, based on the above assumptions, and presented below is more straightforward, the final governing equations are similar to those derived by Larini et al. [22] and implemented by others [17,23,24]. Differences also exist in the numerical approaches and the large-eddy simulation (LES) and filter-based formulation presented here.

The discrete mass source for gas species i due to the thermal degradation of the k th subgrid fuel element is

$$\dot{m}_{k,i}(t) \equiv \int_{S_k(t)} \rho Y_i \mathbf{v}_i \cdot \mathbf{n} dS.$$

We may then define the discrete mass source density as

$$\dot{m}_{k,i}'''(\mathbf{x}, t) \equiv \delta(\mathbf{x} - \mathbf{x}_k[t]) \dot{m}_{k,i}(t). \quad (3)$$

By summing Eq. (3) over all fuel elements, we have the bulk discrete mass source density

$$\dot{m}_{b,i}'''(\mathbf{x}, t) \equiv \sum_k \dot{m}_{k,i}'''(\mathbf{x}, t). \quad (4)$$

Additionally, summing over gas species gives

$$\dot{m}_b'''(\mathbf{x}, t) \equiv \sum_i \dot{m}_{b,i}'''(\mathbf{x}, t). \quad (5)$$

Note that (3)–(5) are discontinuous functions of space.

In principle, a detailed computation of the evolution of each fuel element could be conducted to obtain $\dot{m}_{k,i}(t)$. Here some simplifying assumptions are made to speed the computations. First, we assume that the mass loss for a given fuel element is independent of position within the fuel element (since the element is thermally thin). Thus, gases produced by thermal degradation within a fuel element instantaneously exit at the fuel element surface. Next, within a given computational cell, we assume that fuel elements of the same type have the same thermo-physical properties and evolution. This is consistent with assuming the heat flux environment does not vary within a computational grid cell.

A.2. LES formulation

In LES, the “large” (i.e., resolved) and “small” (i.e., subgrid) scales are formally defined through a low-pass spatial filtering operation. For an arbitrary scalar ϕ we distinguish between two kinds of filtering used to derive the governing equations: conven-

tional filtering to obtain $\bar{\phi}$ and explicit filtering to obtain $\langle \phi \rangle_{V_b}$ (see “special operators” in Section nomenclature for definitions of the filters). Conventional LES quantities are implicitly filtered in the simulation. Explicit filtering uses an anisotropic box filter [38] to determine the bulk source terms due to the presence of subgrid fuel elements. The two filtering operations are equivalent when the implicit-filter kernel is the Heavyside based $G(\mathbf{r}; \Delta) = \frac{1}{V_b} \prod_{i=1}^3 H(\Delta_i/2 - |r_i|)$. For example, consider the filtered bulk mass source term required for the filtered species transport equation. When the conventional filter with the Heavyside kernel is applied to Eq. (4) we obtain

$$\begin{aligned} \overline{\dot{m}_{b,i}'''}(\mathbf{x}, t) &= \int G(\mathbf{x} - \mathbf{x}') \left\{ \sum_k \delta(\mathbf{x}' - \mathbf{x}_k[t]) \dot{m}_{k,i}(t) \right\} d\mathbf{x}', \\ &= \sum_k G(\mathbf{x} - \mathbf{x}_k) \dot{m}_{k,i} = \frac{1}{V_b} \sum_{k \in V_b(\mathbf{x})} \dot{m}_{k,i} = \langle \dot{m}_{b,i}'''(\mathbf{x}, t) \rangle_{V_b}. \end{aligned} \quad (6)$$

The first term on the right-hand-side in Eq. (6) is based on the definition of the conventional filter. The second term follows by the sifting property of the Dirac delta function. In going from the second to the third term we have invoked the Heavyside kernel definition for a cell volume V_b centered at \mathbf{x} (this third term provides the basis for the discrete method used in the numerical implementation). The last term follows from the definition of the explicit filter operator.

Explicit filtering of the discrete drag sources gives

$$\begin{aligned} \langle \mathbf{f}_D''' \rangle_{V_b} &= \frac{1}{V_b} \sum_{k \in V_b} \frac{1}{2} C_{D,k} A_k \bar{\rho} |\mathbf{u}_k - \tilde{\mathbf{u}}| (\mathbf{u}_k - \tilde{\mathbf{u}}) \\ &= \beta_e \sigma_e \frac{3}{8} C_{D,e} \bar{\rho} |\mathbf{u}_e - \tilde{\mathbf{u}}| (\mathbf{u}_e - \tilde{\mathbf{u}}). \end{aligned} \quad (7)$$

The 3/8 factor has also been used in numerical simulations of flame spread through a forest fuel bed [39], Mediterranean shrubs [40], and Australian grassland fires [2]. This factor is 1/8 for a spherical fuel element. The value of the drag coefficient, C_D , depends on the local Reynolds number, Re_e ,

$$C_{D,e} = \begin{cases} 24/Re_e, & Re_e < 1, \\ 24(1 + 0.15Re_e^{0.687})/Re_e, & 1 < Re_e < 1000, \\ 0.44, & 1000 < Re_e, \end{cases} \quad (8)$$

$$Re_e = \frac{2\rho|\mathbf{u}_e - \tilde{\mathbf{u}}|r_e}{\tilde{\mu}} \quad (9)$$

where r_e is the equivalent radius for a sphere $r_e = 3/\sigma_e$. Similar expressions for $C_{D,e}$ have been used previously [41,42]. The correlation for the convective heat transfer coefficient is [43]

$$h_{c,e} = 0.5k(\tilde{T}) \frac{0.683Re_e^{0.466}}{2/\sigma_e}. \quad (10)$$

Here the Reynolds number is based on the relation $\sigma = 2/r$ for cylinders of radius r . We are currently in the initial stages of conducting wind tunnel experiments to test and further refine these empirical drag and heat transfer models for complex arrangements and bulk densities of a variety of vegetation shapes (cylindrical roundwood, flat needles). For this reason, the results presented here should be viewed as a first step that is also in line with contemporary approaches.

The LES filtered equations and subgrid closures adopted for WFDS are presented below, followed by the formulations for combustion chemistry, radiative transport, and pyrolysis (thermal decomposition). Further details of the gas phase model, including the numerical approach, and boundary condition implementation, can be found in McGrattan et al. [12].

A.3. Governing equations

The filtered transport equations for mass, species, momentum, and enthalpy, combined with the equation of state (EOS), shown below in Eqs. (11)–(15), provide $n_s + 5$ independent equations (n_s is the number of species) for $n_s + 5$ unknowns: density, $n_s - 1$ mass fractions, 3 velocity components, hydrodynamic pressure, and enthalpy.

$$\frac{\partial \bar{\rho}}{\partial t} + \nabla \cdot (\bar{\rho} \tilde{\mathbf{u}}) = \langle \dot{m}_b''' \rangle_{V_b} \quad (11)$$

$$\frac{\partial \bar{\rho} \tilde{Y}_i}{\partial t} + \nabla \cdot (\bar{\rho} \tilde{Y}_i \tilde{\mathbf{u}}) = -\nabla \cdot (\tilde{\mathbf{J}}_i + \mathbf{J}_i^{\text{sgs}}) + \langle \dot{m}_{b,i}''' \rangle_{V_b} \quad (12)$$

$$\frac{\partial \bar{\rho} \tilde{\mathbf{u}}}{\partial t} + \nabla \cdot (\bar{\rho} \tilde{\mathbf{u}} \tilde{\mathbf{u}}) = -\nabla \bar{p} - \nabla \cdot (\tilde{\boldsymbol{\tau}} + \boldsymbol{\tau}^{\text{sgs}}) + \bar{\rho} \mathbf{g} + \langle \mathbf{f}_D''' \rangle_{V_b} \quad (13)$$

$$\frac{\partial \bar{\rho} \tilde{h}}{\partial t} + \nabla \cdot (\bar{\rho} \tilde{h} \tilde{\mathbf{u}}) = \frac{\tilde{D}p_0}{\tilde{D}t} - \nabla \cdot (\bar{\mathbf{q}} + \mathbf{q}^{\text{sgs}}) - \nabla \cdot \bar{\mathbf{q}}_r + \langle \dot{q}_{c,b}''' \rangle_{V_b} + \langle \dot{h}_b''' \rangle_{V_b} \quad (14)$$

$$\bar{\rho} = \frac{p_0 \bar{W}}{\tilde{\mathcal{R}} \tilde{T}} \quad (15)$$

Flux and source terms are given below in Tables 4 and 5. Further discussion of the chemistry, radiation, and pyrolysis models follows in Sections A.4, A.5, A.6.

As an important component of the projection method used to solve (11)–(15), a constraint on the velocity divergence is derived by taking the material derivative of the equation of state [44–46]. In the LES context, the filtered material derivative $\tilde{D}/\tilde{D}t$ (see Section nomenclature under “Special operators”) is applied to the filtered EOS, resulting in

$$\begin{aligned} \nabla \cdot \tilde{\mathbf{u}} &= \left(\frac{1}{\bar{\rho} \tilde{c}_p \tilde{T}} - \frac{1}{p_0} \right) \frac{\tilde{D}p_0}{\tilde{D}t} \\ &+ \frac{\bar{W}}{\bar{\rho}} \left(\sum_i \frac{1}{W_i} \left[\overline{\dot{m}_i'''} + \langle \dot{m}_{b,i}''' \rangle_{V_b} - \nabla \cdot (\tilde{\mathbf{J}}_i + \mathbf{J}_i^{\text{sgs}}) \right] \right) \\ &+ \frac{1}{\bar{\rho} \tilde{c}_p \tilde{T}} \left(-\nabla \cdot (\bar{\mathbf{q}} + \mathbf{q}^{\text{sgs}}) - \nabla \cdot \bar{\mathbf{q}}_r + \sum_i \tilde{h}_i \nabla \cdot (\tilde{\mathbf{J}}_i + \mathbf{J}_i^{\text{sgs}}) + \dot{Q}_c''' \right) \\ &+ \frac{1}{\bar{\rho} \tilde{c}_p \tilde{T}} \left(\langle \dot{q}_{c,b}''' \rangle_{V_b} + \langle \dot{h}_b''' \rangle_{V_b} - \sum_i \tilde{h}_i \langle \dot{m}_{b,i}''' \rangle_{V_b} \right). \end{aligned} \quad (16)$$

This constraint is used in the Poisson equation (obtained from the divergence of the momentum equation) for the hydrodynamic pressure. Note that the following relationships – which do not result from straight-forward application of the filter operators – are used to derive (16): $\bar{W} = (\sum_i \tilde{Y}_i / W_i)^{-1}$, $\tilde{c}_p = \sum_i \tilde{Y}_i c_{p,i}$, and $\tilde{h} = \sum_i \tilde{Y}_i \tilde{h}_i$ where $\tilde{h}_i = \Delta h_i^0 + \int_{T_0}^T c_{p,i} dT$. At the open boundaries of the computa-

Table 4

Constitutive relations and subgrid models. Favre-filtered transport coefficients are obtained from molecular coefficients evaluated using filtered temperature and species concentrations, e.g., $\tilde{\mu} = \mu(\mathbf{Y}, \tilde{T})$. The eddy viscosity is obtained from the constant coefficient Smagorinsky model, $\nu_t = (C_s \Delta)^2 |\tilde{\mathbf{S}}|$ with $C_s = 0.2$ and $\Delta = V_b^{1/3}$. The magnitude of the strain rate is $|\tilde{\mathbf{S}}| \equiv (2\tilde{\mathbf{S}} : \tilde{\mathbf{S}})^{1/2}$. The turbulent Schmidt and Prandtl numbers are set to $Sc_t = 0.5$ and $Pr_t = 0.5$, respectively, based on comparisons between FDS and compartment fire experiments [10]. The divergence of the radiative heat flux is included as a source term (see Table 5).

Species flux	$\tilde{\mathbf{J}}_i + \mathbf{J}_i^{\text{sgs}} = -\bar{\rho}(\tilde{D}_i + \frac{\nu_t}{Sc_t}) \nabla \tilde{Y}_i$
Momentum flux	$\tilde{\boldsymbol{\tau}} = -2\tilde{\mu}(\tilde{\mathbf{S}} - \frac{1}{3}(\nabla \cdot \tilde{\mathbf{u}})\mathbf{I})$ $\boldsymbol{\tau}^{\text{sgs},d} \equiv \boldsymbol{\tau}^{\text{sgs}} - \frac{1}{3}\text{trace}(\boldsymbol{\tau}^{\text{sgs}})\mathbf{I} = -2\bar{\rho}\nu_t(\tilde{\mathbf{S}} - \frac{1}{3}(\nabla \cdot \tilde{\mathbf{u}})\mathbf{I})$
Heat flux	$\bar{\mathbf{q}} + \mathbf{q}^{\text{sgs}} = -(\bar{k} + \bar{\rho}\tilde{c}_p \frac{\nu_t}{Pr_t}) \nabla \tilde{T} - \sum_i \bar{\rho}(\tilde{D}_i + \frac{\nu_t}{Pr_t}) \tilde{h}_i \nabla \tilde{Y}_i$

Table 5

Summary of source terms. Details provided in Sections A.4, A.5, A.6.

Water vapor	$\langle \dot{m}_{b,H_2O}'' \rangle_{V_b} = \beta_e \dot{m}_{b,H_2O,e}'',$ See Eq. (30)
Fuel vapor	$\langle \dot{m}_{b,F}'' \rangle_{V_b} = \beta_e \dot{m}_{b,F,e}'',$ See Eq. (31)
Fuel (chemical)	$\dot{m}_F'' = -\frac{\min(\bar{\rho} \bar{V}_F, \bar{\rho} \bar{V}_{O_2}, \bar{r}_{O_2})}{\tau}, \quad \tau = C_{EDC} \frac{\Delta^2 S_{G_i}}{V_F}, \quad C_{EDC} = 0.1$
Drag	$\langle \mathbf{f}_D \rangle_{V_b} = \beta_e \sigma_e \frac{3}{8} C_{D,e} \bar{\rho} \mathbf{u}_e - \bar{\mathbf{u}} (\mathbf{u}_e - \bar{\mathbf{u}})$ See Eq. (7)
Heat release	$\dot{Q}_c'' = -\dot{m}_F'' \Delta \tilde{h}_c$
Radiation	$\nabla \cdot \mathbf{q}_r = \kappa [4\pi I_b(\tilde{T}) - \bar{U}] + \langle \nabla \cdot \mathbf{q}_{r,b} \rangle_{V_b}$ $\langle \nabla \cdot \mathbf{q}_{r,b} \rangle_{V_b} = \kappa_{b,e} [4\pi I_b(T_e) - \bar{U}]$ $\kappa I_b(\tilde{T}) = \max(\chi_r \dot{Q}_c'', \kappa \sigma_B \tilde{T}^4 / \pi)$
Heat transfer	$\langle \dot{q}_{c,b}'' \rangle_{V_b} = \beta_e \sigma_e h_{c,e} (T_e - \tilde{T}),$ See Eq. (10)
Enthalpy	$\langle \dot{h}_b \rangle_{V_b} = \sum_i h_i(T_e) \langle \dot{m}_{b,i}'' \rangle_{V_b}$

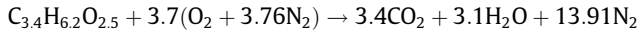
tional domain zero gradient boundary conditions are used for the scalar fields; velocity and pressure boundary conditions are more involved and are described in McGrattan et al. [12].

A.4. Chemical reactions

The molar heat of combustion for a given chemical reaction at constant pressure is [47,48]

$$\Delta H_c \equiv - \sum_i v_i H_i(T) = - \sum_i v_i h_i(T) W_i. \quad (17)$$

where v_i is the stoichiometric coefficient of gas species i ($v < 0$ for reactant species; $v > 0$ for product species). The simplified stoichiometric relation



is used to model the chemical reaction of air and fuel gases generated by wood pyrolysis [31]. In this study, which is focused on fire spread, we do not consider other products such as NOx (N_2 is assumed to be chemically inactive) or secondary reactions. The mass consumption rate for any of the species can be written in terms of a single species. Thus, in terms of the fuel mass consumption rate we have

$$\dot{m}_i'' = r_i \dot{m}_F'', r_i = \frac{v_i W_i}{v_F W_F}, v_F = -1, v_{O_2} = -3.7, v_{CO_2} = 3.4, v_{H_2O} = 3.1. \quad (18)$$

With Eq. (18) the heat release rate per unit volume of the combustion process can be represented in terms of the heat of combustion,

$$\dot{Q}_c'' \equiv - \sum_i \tilde{h}_i \dot{m}_i'' = - \frac{\dot{m}_F''}{v_F W_F} \sum_i v_i \tilde{h}_i W_i = - \frac{\dot{m}_F''}{v_F W_F} \Delta \tilde{h}_c = - \dot{m}_F'' \Delta \tilde{h}_c, \quad (19)$$

where $\Delta \tilde{h}_c = \Delta H_c / W_F$ is the mass-based heat of combustion evaluated at \tilde{T} . The filtered chemical source term \dot{m}_F'' is obtained from the Eddy Dissipation Concept (EDC) model of Magnussen [14], see Table 5.

A.5. Thermal radiation transport

Fires from vegetative fuels are heavily soot laden. Since the radiation spectrum of soot is continuous, it is assumed that the gas behaves as a spectrally independent or gray medium. This results in a significant reduction in computational expense. The vegetative fuel is assumed to be comprised of fixed, uniformly distributed (within the bulk volume V_b), non-scattering, perfectly absorbing, subgrid fuel elements.

Following Consalvi et al. [49], for simplicity the fuel element is assumed to be spherical. The absorption coefficient is [50],

$$\kappa_{b,e} = \frac{1}{4} \frac{\rho_{bv,e}}{\rho_e} \sigma_e = \frac{1}{4} \beta_e \sigma_e \quad (20)$$

This expression for the absorption coefficient has been used in other fire spread models [2,15,16,39,40,51] and has been experimentally validated for vegetative fuels [52]. The final form of the radiation transfer equation (RTE) is then given by

$$\hat{\mathbf{s}} \cdot \nabla \bar{I}(\mathbf{x}, \hat{\mathbf{s}}) = \kappa [I_b(\tilde{T}) - \bar{I}(\mathbf{x}, \hat{\mathbf{s}})] + \kappa_{b,e} [I_b(T_e) - \bar{I}(\mathbf{x}, \hat{\mathbf{s}})]. \quad (21)$$

A table containing the values of κ as a function of species mass fractions and temperature for a given mixture of participating gaseous species (H_2O , CO_2) and soot particulate is computed before the simulation begins. A soot evolution model is not used. Instead, the mass of soot generated locally is an assumed fraction, χ_s , of the mass of fuel gas consumed by the combustion process. In the WFDS simulations reported here, $\chi_s = 0.02$ is used. Values of χ_s for Douglas fir range from less than 0.01 to 0.025 under flaming conditions [35].

Integrating the RTE (21) over all solid angles gives the equation for conservation of radiant energy,

$$\begin{aligned} \nabla \cdot \mathbf{q}_r(\mathbf{x}) &= \kappa [4\pi I_b(\tilde{T}) - \bar{U}(\mathbf{x})] + \kappa_{b,e} [4\pi I_b(T_e) - \bar{U}(\mathbf{x})] \\ &= \kappa [4\pi I_b(\tilde{T}) - \bar{U}(\mathbf{x})] + \langle \nabla \cdot \mathbf{q}_{r,b} \rangle_{V_b}. \end{aligned} \quad (22)$$

where \bar{U} is the integrated radiation intensity. Eq. (22) is required in the enthalpy transport Eq. (14) and in the divergence constraint Eq. (16).

Capturing the effects of subgrid heterogeneity of the flame temperature requires special treatment of the radiation emission term κI_b since this term depends on the fourth power of the local temperature. In regions where the local mean temperature is lower and spatial gradients of scalars are sufficiently resolved, capturing the effects of the subgrid temperature distribution is less critical. For this reason, we model the gas phase emission term as

$$\kappa I_b(\tilde{T}) = \max(\chi_r \dot{Q}_c'', \kappa \sigma_B \tilde{T}^4 / \pi), \quad (23)$$

where χ_r is the fraction of the chemical heat release rate per unit volume that is radiated to the local volume surrounding the flame region. Note that some of this radiation will be absorbed by the surrounding soot and vegetative fuel. As a result, for sufficiently smoke laden fires the fraction of chemical heat release radiated to a location outside the smoke plume will be smaller than the local value. For hydrocarbon pool fires the local value is $\chi_r \approx 0.30$ – 0.35 while the global value is less, 0.10 [53]. In wood cribs $\chi_r \approx 0.20$ – 0.40 [34]. The value used in the simulations presented here is $\chi_r = 0.35$.

A finite volume method based on that of Raithby and Chui [54] is used to solve the gray gas form of (21). It requires approximately 20% of the total CPU time. The spatial discretization of the radiation transport equation is the same as that used in the other gas-phase conservation equations.

A.6. Thermal decomposition of vegetative fuel

In this section we provide the details for obtaining the bulk mass source terms $\langle \dot{m}_{b,i}'' \rangle_{V_b}$ for water vapor ($i = H_2O$) and fuel vapor ($i = F$) required in the mass, species, and enthalpy transport equations.

The model for the thermal degradation of a thermally-thin vegetative fuel used here is similar to that employed by others (e.g., [43]) and previously in WFDS simulations of fire spread in grassland fuels [2]. The equation governing the temperature of a thermally thin fuel element, k , is

$$\rho_k c_{p,k} \frac{dT_k}{dt} = -\Delta h_{vap} \dot{m}_{H_2O,k}'' - \Delta h_{pyr} \dot{m}_{F,k}'' - \nabla \cdot \mathbf{q}_{c,k} - \nabla \cdot \mathbf{q}_{r,k}. \quad (24)$$

Applying the explicit spatial filter gives

$$\rho_{e,b} c_{p,e} \frac{dT_e}{dt} = -\Delta h_{\text{vap}} \langle \dot{m}_{b,\text{H}_2\text{O}}''' \rangle_{V_b} - \Delta h_{\text{pyr}} \langle \dot{m}_{b,F}''' \rangle_{V_b} - \langle \dot{q}_{c,b}''' \rangle_{V_b} - \langle \nabla \cdot \mathbf{q}_{r,b} \rangle_{V_b}. \quad (25)$$

The third and fourth terms on the right-hand-side of Eq. (25) are the fuel element bulk contributions from unresolved conduction and radiative heat transfer (see Table 5).

In the solid phase model the bulk density and specific heat and have contributions from dry virgin vegetative fuel and moisture,

$$\rho_{e,b} = \rho_{bv} + \rho_{b,\text{H}_2\text{O}} \quad (26)$$

$$c_{p,e} = \frac{\rho_{bv} c_{p,v} + \rho_{b,\text{H}_2\text{O}} c_{p,\text{H}_2\text{O}}}{\rho_b} \quad (27)$$

where initially $\rho_{e,b,\text{H}_2\text{O}} = M_e \rho_{bv}$, note that here M_e is a fraction not a percent.

The temperature Eq. (25) for the fuel bed is solved assuming a two stage endothermic decomposition process (water evaporation followed by solid fuel volatilization). This results in a mass loss of vegetative fuel:

$$\frac{d\rho_{e,b}}{dt} = \langle \dot{m}_{e,b}''' \rangle_{V_b} = \langle \dot{m}_{b,\text{H}_2\text{O}}''' \rangle_{V_b} + \langle \dot{m}_{b,F}''' \rangle_{V_b}. \quad (28)$$

With the net heat flux divergence defined as

$$\langle \dot{q}_{e,\text{net}}''' \rangle_{V_b} \equiv -\langle \dot{q}_{c,b}''' \rangle_{V_b} - \langle \nabla \cdot \mathbf{q}_{r,b} \rangle_{V_b} \quad (29)$$

the thermal degradation model used here is given by the following:

$$\langle \dot{m}_{e,b,\text{H}_2\text{O}}''' \rangle_{V_b} = \beta_e \dot{m}_{e,\text{H}_2\text{O}}''' = \begin{cases} 0, & T_e < 100^\circ\text{C}, \\ \frac{\langle \dot{q}_{\text{net}}''' \rangle_{V_b}}{\Delta h_{\text{vap}}}, & T_e = 100^\circ\text{C}, \quad \rho_{b,\text{H}_2\text{O}} V_b > 0, \quad \langle \dot{q}_{\text{net}}''' \rangle_{V_b} > 0 \end{cases} \quad (30)$$

$$\langle \dot{m}_{e,b,F}''' \rangle_{V_b} = \beta_e \dot{m}_{e,F}''' = \begin{cases} 0, & T_e < 127^\circ\text{C}, \\ \frac{\langle \dot{q}_{\text{net}}''' \rangle_{V_b}}{\Delta h_{\text{pyr}}} \left(\frac{T_e - 127}{100} \right), & 127^\circ\text{C} \leq T_e \leq 227^\circ\text{C}, \\ \frac{\langle \dot{q}_{\text{net}}''' \rangle_{V_b}}{\Delta h_{\text{pyr}}}, & T_e \geq 227^\circ\text{C}, \\ \text{for all cases} & \rho_{b,F} V_b > \chi_{e,\text{char}} \rho_{bv} V_b, \quad \langle \dot{q}_{\text{net}}''' \rangle_{V_b} > 0 \end{cases} \quad (31)$$

where $\chi_{e,\text{char}}$ is the char fraction for fuel elements of type e . The heat of vaporization for water is $\Delta h_{\text{vap}} = 2259 \text{ kJ kg}^{-1}$ and the heat of pyrolysis is $\Delta h_{\text{pyr}} = 416 \text{ kJ kg}^{-1}$ [40] (also see Table 3). The initial temperature $T_e(t_0)$ is ambient or user defined.

The temperature of the vegetative fuel evolves according to Eq. (25), which was also used (up to the point of pyrolysis) by Albini [15,16]. Once T_e reaches the boiling temperature it is assumed that drying requires all of the available heat so that $T_e = 100^\circ\text{C}$ until all the moisture has evaporated. After all the moisture has been removed, the temperature of the fuel element evolves according to Eq. (25) with $\langle \dot{m}_{b,\text{H}_2\text{O}}''' \rangle_{V_b} = 0$. With a net influx of heat, T_e continues to rise, eventually reaching a temperature $T_e = 127^\circ\text{C}$, when pyrolysis begins. The model for solid fuel thermal degradation uses the temperature dependent mass loss rate expression of Morvan et al. [40]. This fuel volatilization model is based on thermogravimetric analysis of a number of vegetation species [55,56]. Since char oxidation is not modeled, smoldering or glowing combustion is not accounted for.

References

- [1] E.A. Johnson, K. Miyanishi (Eds.), *Forest Fires: Behavior and Ecological Effects*, Academic Press, 2001.
- [2] W.E. Mell, M.A. Jenkins, J. Gould, P. Cheney, A physics based approach to modeling grassland fires, *Int. J. Wildland Fire* 16 (2007) 1–22.
- [3] R.C. Rothermel, A mathematical model for predicting fire spread in wildland fuels, Technical Report 1972.
- [4] P.L. Andrews, C.D. Bevins, R.C. Seli, BehavePlus fire modeling system, version 2.0: User's Guide, Technical Report USDA For. Serv. Gen. Tech. Rep. RMRS-GTR-106WWW, USDA Forest Service, 2003. 132 pp. <<http://fire.org>>.
- [5] M.A. Finney, FARSITE: Fire Area Simulator-Model, Development and Evaluation, Technical Report RMRS-RP-4, USDA Forest Service, Rocky Mountain Research Station Paper, 1998.
- [6] R.G. Rehm, W.E. Mell, A simple model for wind effects of burning structures and topography on WUI surface-fire propagation, *Int. J. Wildland Fire* 18 (2009) 290–301.
- [7] National Fire Protection Association, Standard for reducing structure ignition hazards from wildland fires, Technical Report NFPA 1144, NFPA, 1 Batterymarch Park, Quincy, MA 02169-7471, 2008.
- [8] Inc. International Code Council, International wildland-urban interface code, Technical Report, Publications, 4051 West Flossmoor Road, Country Club Hills, IL, 60478, January 2006.
- [9] W.E. Mell, S.L. Manzello, A. Maranghides, D. Butry, R.G. Rehm, Wildland-urban interface fires: current approaches and research needs, *Int. J. Wildland Fire*, in press.
- [10] K.B. McGrattan, S. Hostikka, J. Floyd, B. Klein, Fire Dynamics Simulator Technical Reference Guide, Validation, vol. 2, Technical Report NISTIR Special Publication, 1018-5, National Institute of Standards and Technology, Gaithersburg, Maryland, September 2008. <<http://fire.nist.gov/fds>>.
- [11] R. McDermott, K.B. McGrattan, S. Hostikka, J. Floyd, Fire Dynamics Simulator Technical Reference Guide, Verification, vol. 3, Technical Report NISTIR Special Publication, 1018-5, National Institute of Standards and Technology, Gaithersburg, Maryland, September 2008. <<http://fire.nist.gov/fds>>.
- [12] K.B. McGrattan, S. Hostikka, J. Floyd, H. Baum, Rehm R., W. Mell, R. McDermott, Fire Dynamics Simulator Technical Reference Guide, Mathematical Model, vol. 1, Technical Report NISTIR Special Publication, 1018-5, National Institute of Standards and Technology, Gaithersburg, Maryland, September 2008. <<http://fire.nist.gov/fds>>.
- [13] K.B. McGrattan, B. Klein, S. Hostikka, J. Floyd, Fire Dynamics Simulator Technical User's Guide. Technical Report NISTIR Special Publication, 1018-5, National Institute of Standards and Technology, Gaithersburg, Maryland, September 2008. <<http://fire.nist.gov/fds>>.
- [14] B.F. Magnussen, B.H. Hjertager, On mathematical modeling of turbulent combustion with special emphasis on soot formation and combustion, in: *Proc. Combust. Inst.*, vol. 16, 1976, pp. 719–729.
- [15] F.A. Albini, A model for fire spread in wildland fuels by radiation, *Combust. Sci. Technol.* 42 (1985) 229–258.
- [16] F.A. Albini, Wildland fire spread by radiation – a model including fuel cooling by natural convection, *Combust. Sci. Technol.* 45 (1986) 101–113.
- [17] J.L. Dupuy, D. Morvan, Numerical study of the a crown fire spreading toward a fuel break using a multiphase physical model, *Int. J. Wildland Fire* 14 (2005) 141–151.
- [18] R. Linn, J. Reisner, J.J. Colman, J. Winterkamp, Studying wildfire behavior using FIRETEC, *Int. J. Wildland Fire* 11 (2002) 233–246.
- [19] P.G. Jarvis, G.B. James, J.J. Lansberg, *Vegetation and the Atmosphere*, Case studies, vol. 2, Academic Press, New York, 1976, pp. 172–240 (Chapter 7. Coniferous Forest).
- [20] S.L. Manzello, A. Maranghides, W.E. Mell, Firebrand generation from burning vegetation, *Int. J. Wildland Fire* 16 (2007) 458–462.
- [21] S.L. Manzello, J.R. Shields, T.G. Cleary, A. Maranghides, W.E. Mell, J.C. Yang, Y. Hayashi, D. Nii, T. Kurita, On the development and characterization of a firebrand generator, *Fire Safety J.* 43 (2008) 258–268.
- [22] M. Larini, F. Giroud, B. Porterie, J.-C. Loraud, A multiphase formulation for fire propagation in heterogeneous combustible media, *Int. J. Heat Mass Transfer* 41 (1998) 881–897.
- [23] B. Porterie, J.L. Consalvi, A. Kaiss, J.C. Loraud, Predicting wildland fire behavior and emissions using a fine-scale physical model, *Numer. Heat Transfer, Part A* 47 (2005) 571–591.
- [24] X. Zhou, S. Mahalingham, D. Weise, Experimental study and large eddy simulation of the effect of terrain slope on marginal burning in shrub fuel beds, *Comb. Sci. Tech.* 31 (2007) 2547–2555.
- [25] P.J. Pagni, Causes of the 20th October Oakland Hills conflagration, *Fire Safety J.* 21 (1993) 331–340.
- [26] F.A. Albini, Transport of firebrands by line thermals, *Combust. Sci. Technol.* 32 (1983) 277–288.
- [27] V. Babrauskas, *The SFPE Handbook of Fire Protection Engineering*, fourth ed., National Fire Protection Assoc., Quincy, MA, 2008.
- [28] R.C. Rothermel, *Thermal Uses and Properties of Carbohydrates and Lignins*, Chapter Forest Fires and the Chemistry of Forest Fuel, Academic Press, San Francisco, 1976. pp. 245–259.
- [29] B.J. Stocks, M.E. Alexander, B.M. Wotten, C.N. Steffner, M.D. Flannigan, S.W. Taylor, N. Lavoie, J.A. Mason, G.R. Hartley, M.E. Maffey, G.N. Dalrymple, T.W. Blake, M.G. Cruz, R.A. Lanoville, Crown fire behavior in a northern jack pine – black spruce forest, *Can. J. Forest Res.* 34 (2004) 1548–1560.
- [30] N.P. Cheney, J.S. Gould, W.R. Catchpole, The influence of fuel, weather and fire shape variables on fire spread in grasslands, *Int. J. Wildland Fire* 3 (1) (1993) 31–44.
- [31] S.J. Ritchie, K.D. Steckler, A. Hamins, T.G. Cleary, J.C. Yang, T. Kashiwagi, The effect of sample size on the heat release rate of charring materials, in: *International Association for Fire Safety Science*, March 3–7, 1997, pp. 177–188.
- [32] R.A. Susott, Characterization of the thermal properties of forest fuels by combustible gas analysis, *Forest Sci.* 2 (1982) 404–420.

- [33] W.J. Parker, Prediction of the heat release rate of Douglas fir, in: International Association for Fire Safety Science, Hemisphere, Publishing, New York, 1998, pp. 337–346.
- [34] J.G. Quintiere, Principles of Fire Behavior, Delmar Publishers, Albany, 1997.
- [35] C.P. Bankston, B.T. Zinn, R.F. Browner, E.A. Powell, Aspects of the mechanisms of smoke generation by burning materials, *Combust. Flame* 41 (1981) 273–292.
- [36] F.P. Incropera, D.P. Dewitt, Fundamentals of Heat and Mass Transfer, fourth ed., John Wiley & Sons, New York, 1996. p. 846.
- [37] S.B. Pope, Computations of turbulent combustion: progress and challenges, in: *Proc. Comb. Inst.*, vol. 30, 1990, pp. 591–612.
- [38] S.B. Pope, *Turbulent Flows*, Cambridge, 2000.
- [39] D. Morvan, J.L. Dupuy, Modeling fire spread through a forest fuel bed using a multiphase formulation, *Combust. Flame* 127 (2001) 1981–1984.
- [40] D. Morvan, J.L. Dupuy, Modeling the propagation of a wildfire through a Mediterrean shrub using a multiphase formulation, *Combust. Flame* 138 (2004) 199–210.
- [41] B. Porterie, D. Morvan, J.C. Loraud, M. Larini, Firespread through fuel beds: modeling of wind-aided fires and induced hydrodynamics, *Phys. Fluids* 12 (7) (2000) 1762–1782.
- [42] R.G. Rehm, K.B. McGrattan, H.R. Baum, Large eddy simulation of flow over a wooded building complex, *Wind Struct.* 5 (2002) 291–300.
- [43] B. Porterie, D. Morvan, M. Larini, J.C. Loraud, Wildfire propagation: a two-dimensional multiphase approach, *Combust. Explo. Shock Waves* 34 (1) (1998) 139–150, also in *Fizika Goreniya i Vzryva*, vol. 34, p.26, 1998.
- [44] J. Bell, AMR for low Mach number reacting flow, Lawrence Berkeley National Laboratory Paper LBNL-54351, 2004.
- [45] W.E. Mell, K.B. McGrattan, H.R. Baum, g-jitter effects on spherical diffusion flames, *Microgravity Sci. Technol.* 15 (2004) 12–30.
- [46] R. McDermott, K. McGrattan, W.E. Mell, Derivation of the velocity divergence constraint for low-mach flow solvers, NIST Technical Note, 2007, p. 1487.
- [47] N. Peters, *Turbulent Combustion*, Cambridge University Press, Cambridge, UK, 2000.
- [48] T. Poinso, D. Veynante, *Theoretical and Numerical Combustion*, second ed., Edwards, 2005.
- [49] J.L. Consalvi, B. Porterie, J.C. Loraud, Model of radiative heat transfer in particulate medium, *Int. J. Heat Mass Transfer* 45 (2002) 2755–2768.
- [50] NAS, A Study of Fire Problems, National Academy of Sciences – National Research Council, Washington, DC, 1961. Chapter Appendix IV: Note on radiative transport problems arising in fire spread, Publication 949.
- [51] N.J. De Mestre, E.A. Catchpole, D.H. Anderson, R.C. Rothermel, Uniform propagation of a planar fire front without wind, *Combust. Sci. Technol.* 65 (1989) 231–244.
- [52] B.W. Butler, in: *Proceedings: 12th Conference of Fire and Forest Meteorology*, 1993, p. 26.
- [53] H. Koseki, G.W. Mulhooand, The effect of diameter of the burning of crude oil pool fires, *Fire Technol.* 27 (1991) 54–65.
- [54] G.D. Raithby, E.H. Chui, A finite-volume method for predicting radiant heat transfer in enclosures with participating media, *J. Heat Transfer* 112 (2) (1990) 415–423.
- [55] A.P. Dimitrakipoulos, Pyric properties of some dominant Mediterranean vegetation species, *J. Anal. Appl. Pyrol.* 60 (2001) 123.
- [56] C. Moro, Technical Report, Technical report, INRA Equipe de Prêdes Incendies de Forêt, 1997.